Master Thesis

Nb based Josephson Junctions: Subgap transport phenomena

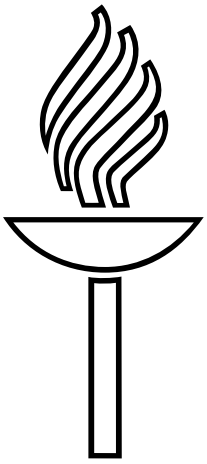

Ari Halvari

16th September 2005

NanoScience Center
Department of Physics
University of Jyväskylä

Acknowledgements

This work has been carried out at the Department of Applied Physics, University of Jyväskylä.

I wish to thank my supervisors Dr. Sorin Paraoanu and Dr. Jussi Toppari for their guidance, and for their extreme patience. I'm also grateful to Mr Mohamed Hassan, a true friend in need.

Jyväskylä 16th September 2005

Ari Halvari

Contents

1 Introduction **1**

2 Tunneling phenomenon **3**

2.1 Tunneling 3

2.1.1 Energy-gap $\Delta(T)$ 5

2.1.2 Density of states and Fermi-Dirac distribution 6

2.1.3 NIN-tunneling 8

2.1.4 NIS-tunneling 10

2.1.5 SIS-tunneling 11

2.1.6 Supercurrent 12

2.2 Josephson transistor 14

2.2.1 Good quantum variables for the Josephson transistor 15

2.2.2 Three-band model of the Josephson transistor 17

2.2.3 Niobium based Josephson junctions 18

3 Sample fabrication **22**

3.1 Preparation of the sample 23

3.2 Resists 24

3.3 Dose determination 24

3.4 Evaporation 27

4 Measurements **30**

4.1 Critical temperature T_c^{Nb} 31

4.2 Charging energy 32

4.3 Characteristics of the samples 33

5 Subgap transport phenomena **36**

5.1 Resonant tunneling of Cooper pairs 38

5.2 Elastic cotunneling of quasiparticles, q-MQT 40

5.3 Smearing of the gap 44

5.4 Conclusion 45

6 Further improvements **47**

6.1 Suspended single-electron transistor 48

6.2 Fabrication of SUSET 48

6.3 Measurement of SUSET 51

6.4 Conclusion of Suset 53

Bibliography 54

Appendix **59**

Chapter 1

Introduction

The field of single charge tunneling phenomena and superconducting devices has opened a new demand on high performance nanofabrication techniques. In the past years there has been a strong motivation to develop a technique for the reliable fabrication of a small sized, Nb-based Josephson junction, because of large superconducting gap of Nb. Until now, the conventional shadow evaporation technique known as the self-alignment technique has been applied succesfully for soft metals like Al, Cu and Pb. For the refractory metals like Nb it is known to be difficult to apply. The self-alignment technique providing nanoscale accuracy is commonly used with the polymethylmethacrylate (PMMA) and the co-polymer [P(MMA-MAA)], containing PMMA and methacrylic acid monomers (MAA), resist as a double layer stencil mask.

There are basically two different methods to fabricate submicron Nb-based tunnel junctions. One is the self-alignment with a stencil mask *in situ* [3, 6, 7] and the second one is the multilayer technique by which the layers are formed *in situ*, followed by process *ex situ* [5]. The need for different fabrication processes is caused by the poor quality of Nb film evidencing as their transition temperature T_c being far below the bulk value. This degration of the film is believed to be due to the contamination of the Nb layer by outgassing from the resists during the evaporation [8]. For this problem the authors in [6] used thermostable trilayer resist Phenylene-ether-suofone (PES) polymere which has a glass temperature and decomposition temperature much higher than those of PMMA resist. By fabricating Nb wire with this process they reached T_c of 7.1

K. However the process itself is more complicated than conventional PMMA process. Even more complicated method is developed by authors of [5]. Advantage of this process is the reliability of the insulating layer and the high-quality superconducting Nb-electrode. Disadvantage is the complicateness of the process which makes it more difficult to reduce the size of the junction below (300×300) nm.

There has been several reports on the fabrication of superconducting single-electron devices using Niobium. Almost all of them has come to a conclusion, that it is not possible to fabricate high quality Nb-based devices using shadow evaporation technique with PMMA as a resist. Instead other methods have been developed. Therefore it is more than welcomed to demonstate that high-quality submicron Nb-based devices can be fabricated using conventional e-beam lithography methods. Inspired by an exciting idea to create heterostructures with Nb island connected through Al leads, i.e., the Nb acting as an energy barrier for undesirable quasiparticles reducing the poisoning effect [44], it will be shown in this thesis, that it is possible to fabricate good quality Nb-Al junctions using conventional PMMA-P(MMA-MAA) resists as a stencil mask [56]. With single electron transistor geometry and single Nb-Al junctions appearing transition temperature T_c of 8.54 K and a gap energy up to $\Delta_{\mathrm{Nb}} = 1.46$ meV was achieved. Furthermore, the measured $\mathrm{Al/AlO_X/Nb/AlO_X/Al}$ SSETs (Superconducting Single Electron Transistor) showed clear signature of the resonant tunneling of Cooper pairs combined with the elastic cotunneling of quasiparticles, q-MQT, through the barrier of Δ_{Nb} [51], since the inelastic cotunneling $I_{\mathrm{inelastic}} \propto e^{-D(T)/k_{\mathrm{B}}T}$ is exponentially reduced leaving the elastic one as only possible tunneling process.

Chapter 2

Tunneling phenomenon

2.1 Tunneling

What is meant by a quantum mechanical tunneling is the particle penetration through a classically forbitten area. The α decay of radioactive nuclei through a potential wall, formed by very short range nuclear attraction and Coulomb interaction, is one example of the barrier penetration. As a simple mathematical example which describes the tunneling behaviour of particles can be examined considering the one dimensional potential

$$U(x) = \begin{cases} V_0 & \text{, when } |x| < a \\ 0 & \text{, otherwise} \end{cases} \tag{2.1}$$

and assuming that the mono-energetic source of particles is situated in direction $x < -\infty$. Classically particles´ total energy $E < V_0$ would indicate all of them being reflected from the left-hand edge ($x < -a$). Quantum-mechanically the situation is very different. As a consequence of a particle´s wave property the time independent Schrödinger equation

$$-\frac{\hbar^2}{2m}\nabla^2\psi(x) + U(x)\psi(x) = E\psi(x), \tag{2.2}$$

qives a non-classical solution. The solutions in the outer regions are

$$\begin{aligned} \phi &= Ae^{ikx} + A'e^{-ikx} && x < -a \\ \phi &= Ce^{ikx} && x > a \end{aligned}$$

where the two different terms, at $x < -a$, corresponds to incident and reflected particles. If restricted to situation $E < V_0$ the solution of the Schrödinger equation (2.2) inside the barrier is of the form [4]

$$\phi = Be^{-\kappa x} + B'e^{\kappa x}, \tag{2.3}$$

where

$$\kappa = \sqrt{\frac{2m}{\hbar^2}(V_0 - E)}.$$

Finally the four unknown constants A', B, B' and C are determined by matching wave equations (2.1) and (2.3) at the boundaries $x = \pm a$, and requiring continuity of ϕ and $d\phi/dx$. The transmission coefficient T, indicating probability that a particle penetrates through the barrier, is obtained from the ratio of incident and passing amplitudes. In a limit $\kappa a \gg 1$

$$T = \left|\frac{C}{A}\right|^2 \approx e^{-4\kappa a}\left(\frac{\kappa x}{k^2 + \kappa^2}\right)^2. \tag{2.4}$$

From the equation (2.4), which disagrees with classical physics, it can be seen that a particle have a small probability to tunnel through the barrier of height $V_0 > E$. The probability decreases as the height V_0 or the thickness of the barrier increases.

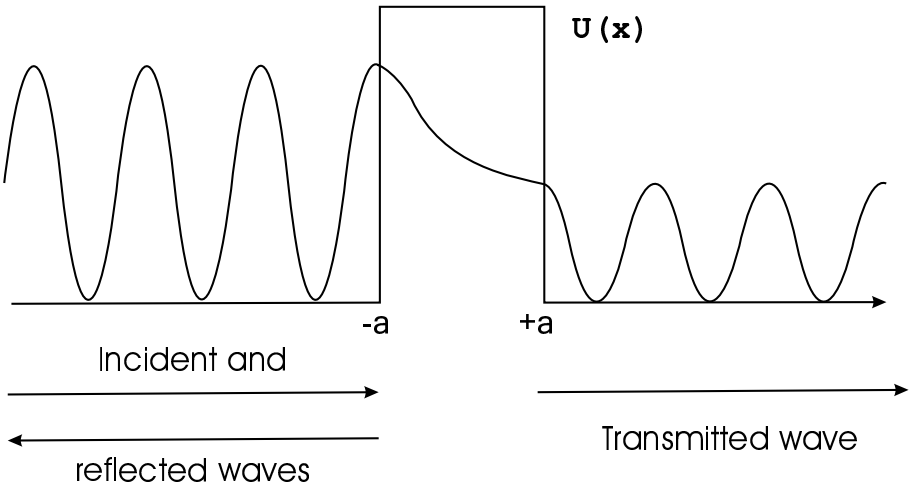

Figure 2.1: *The wave function penetrates through a potential barrier*

Tunnel junction can be fabricated by two conductors separated by a thin insulating layer. This capacitively connected structure represents a condensator according to the classical physics but as the thickness of the insulator is reduced it forms a potential

wall which still allows conduction electrons to tunnel through the barrier according to the laws of quantum mechanics. This is what is called a tunnel junction and it can be treated as any electrical component. In this thesis a tunnel junction is treated in limiting conditions (partly at sub-Kelvin regime) where the used conductors turn into superconducting state with disappearance of electrical resistance. In addition, the energy-gap of superconductor makes the current-voltage dependence of a junction very complicated.

2.1.1 Energy-gap $\Delta(T)$

Transition of a metal from the normal state to the superconducting state has the property of a condensating the electrons close to the Fermi level into a bosonic state and leaving a band of forbidden states around it. A key conceptual element is the pairing of electrons into bosonic Cooper pairs which behaves drastically different from the single electrons that are fermions and obeys Pauli exclusion principle. According to the **BCS**-theory the condensation of the electrons relieves energy $\Delta(T)$ per electron. The total binding energy of the Cooper pair is then $2\Delta(T)$. As the temperature increases the energy gap $\Delta(T)$ decreases. The effect of condensation is illustrated in occupation energy level diagram in figure (2.2).

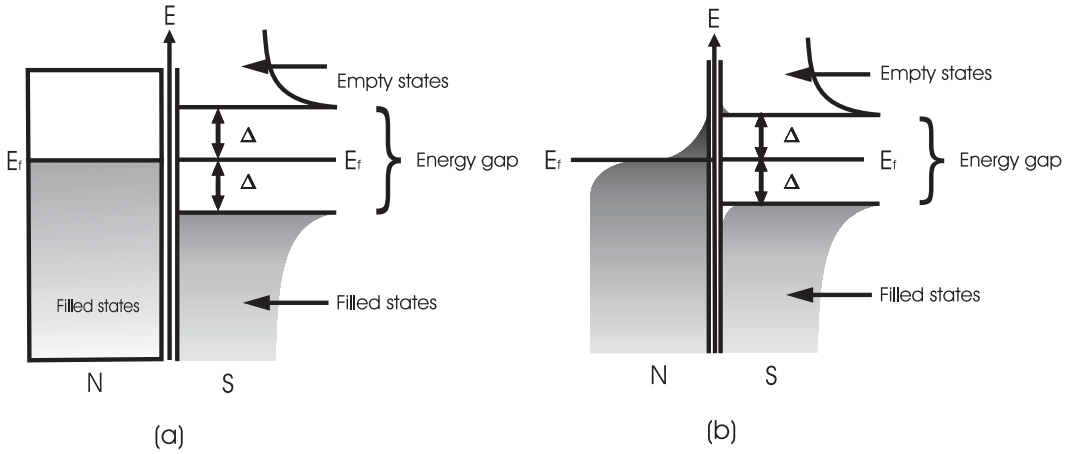

Figure 2.2: *The energy diagram gives the electron occupation according to the Fermi-Dirac distribution at (a) $T = 0$ and at (b) $T > 0$. The normal metal is marked with N and the superconductor with the gap of width 2Δ is marked with S*

In order to break a Cooper pair the energy $2\Delta(T)$ is needed. Also adding one extra electron to a superconductor increases the energy of the system at least the value of $\Delta(T)$. That is, a single extra electron is not allowed to be at the gap level and must therefore occupy the first empty level available above the gap (figure 2.2b). In both cases, normal and superconducting, the single electron states which are vacant at absolute zero are occupied according to **Fermi-Dirac distribution**. These electrons are denoted as *quasiparticles*.

In addition, quasi-electrons below the gap can be excited with the minimum energy of $2\Delta(T)$ above the gap, leaving vacant states as seen in figure (2.2b). One of the predictions of the BCS theory was the minimum energy needed to break a pair and create two quasiparticle excitations [1]. The energy was predicted to increase from zero, at transition temperature T_{C}, to a maximum value

$$\Delta(0) = 1.76 k_{\mathrm{B}} T_{\mathrm{C}}. \tag{2.5}$$

Near T_{C}, $\Delta(T)$ drops to zero approximately as

$$\frac{\Delta(T)}{\Delta(0)} \approx 1.74\sqrt{1 - \frac{T}{T_{\mathrm{C}}}}. \tag{2.6}$$

So besides the temperature T the gap width is comparable to T_{C}, the critical temperature, at which the superconductor turns into normal metal. This is very essential result from the point of view of fabricating good quality Josephson junctions as can be seen later in this thesis.

2.1.2 Density of states and Fermi-Dirac distribution

Fermi-Dirac distribution $f(E)$ gives the probability that the electron state with energy E is occupied,

$$f(E) = \frac{1}{e^{\frac{E-\mu}{k_{\mathrm{B}}T}} + 1}. \tag{2.7}$$

When fermilevel E_{F} is chosen as zero energy level and $\mu \simeq E_{\mathrm{F}}$, equation (2.7) can be written as

$$f(E) = \frac{1}{e^{\frac{E}{k_{\mathrm{B}}T}} + 1}. \tag{2.8}$$

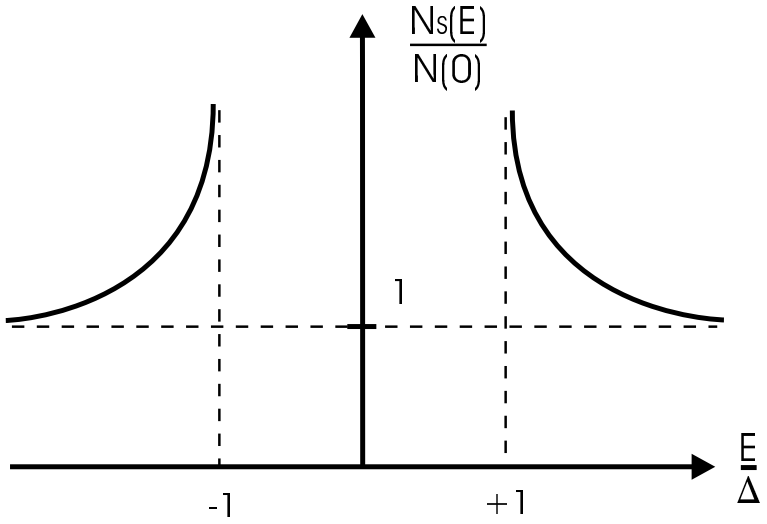

Figure 2.3: *Density of states in superconducting compared to normal state.*

Especially when $T = 0$

$$f(E) = \begin{cases} 1 & \text{, when } E < 0 \\ 0 & \text{, when } E > 0. \end{cases} \tag{2.9}$$

Furthermore to achieve the actual occupation of the energy levels the **density of states**,$N(E)$, is needed. For normal metal this reads

$$N_{\mathrm{n}}(E) = \frac{\sqrt{2}m^{\frac{3}{2}}}{\pi^2\hbar^3}\sqrt{E}, \tag{2.10}$$

and it tells the amount of quasiparticle states per unit energy. Based on the fact that electrons cannot be vanished the number of states must coincide with the superconductor outside the gap, i.e,

$$N_{\mathrm{s}}(E)dE = N_{\mathrm{n}}(\xi)d\xi, \tag{2.11}$$

where ξ describes the squared energy difference from the gap edge. BCS-theory defines the elementary quasiparticle excitations of the system as

$$E = \sqrt{\xi^2 + |\Delta|^2}, \tag{2.12}$$

which leads to

$$\xi = \sqrt{E^2 - \Delta^2}. \qquad (|E| > \Delta)$$

Concerning interest with energies ξ only a few electronvolts from the Fermi energy, the density of states can be taken as constant $N_{\mathrm{n}} = N(0)$. This leads directly to result

$$\frac{N_{\mathrm{s}}(E)}{N(0)} = \frac{d\xi}{dE} = \begin{cases} \frac{|E|}{\sqrt{E^2-\Delta^2}} & (|E| > \Delta) \\ 0 & (|E| < \Delta) \end{cases} \tag{2.13}$$

As a result of equation (2.13) there is a divergent state density just outside $E = \Delta$. But when integrated over the energy spectrum the total number of states is conserved. However, it has a strong effect on current-voltage behavior, which can be used, e.g., in technique known as the tunneling spectroscopy [2]. Following sections illustrates the examination of the energy gap and the density of states provided by electron tunneling.

2.1.3 NIN-tunneling

Since the probability of tunneling (eq: 2.4) exists, obviously the barrier has a finite resistance. Let's look at the current-voltage behaviour of the normal metal-insulator-normal metal (NIN). At $T = 0$ all states up to E_{f} are filled. Without bias voltage

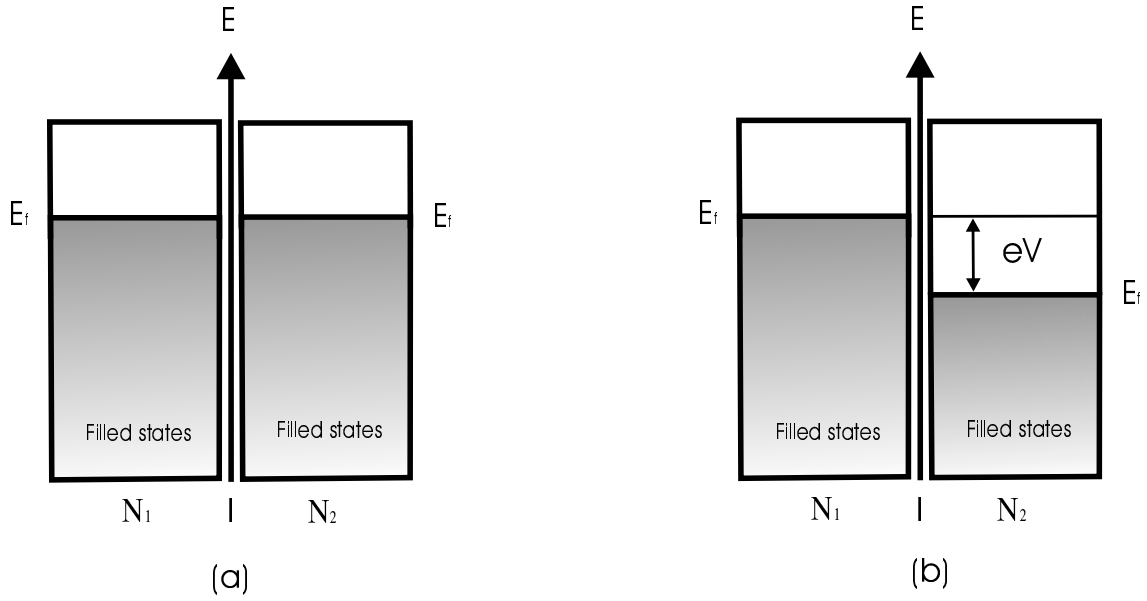

Figure 2.4: *Energy level diagram at zero temperature (a) without bias voltage and (b) with bias voltage.*

the Fermi-surfaces are at even and no tunneling occur (fig: 2.4a). When negative

potential difference V is applied over the junction the energy of the left-hand sided electrons increases the amount of eV compared to the right-hand sided. This enables electrons to tunnel to the right-hand electrode creating an electric current to the left (fig:2.4b). With this model tunneling transitions are horizontal, i.e., they occur at constant energy after adjusting their relative energies according to the applied voltage [1]. This simplifies the calculations greatly. The current is directly proportional to the amount of occupied states inside the energy band with width of dE, $N_1(E-eV)f(E-eV)dE$ in the left-hand electrode, and the vacant states $N_2(E)(1-f(E))dE$ in the right-hand side electrode. The zero energy level has been chosen as Fermi-level at the right-hand side electrode. Obviously the current is proportional to the transmission coefficient $|T|$ and some constant of proportionality A. The factor $T(E)$ is assumed to be constant for small bias voltages and at low temperature, therefore probabilities $T_{1\to2}$ and $T_{2\to1}$ are equal. This is a fair approximation [10] at sub-Kelvin regime, and thus the tunneling current $1 \to 2$ in the energy interval dE can be written as

$$dI_{1\to2} \propto A|T|^2 N_1(E-eV)N_2(E)f(E-eV)[1-f(E)]dE.$$

Correspondingly tunneling $2 \to 1$ can be written in the form

$$dI_{2\to1} \propto A|T|^2 N_1(E-eV)N_2(E)f(E)[1-f(E-eV)]dE$$

Subtracting the reverse current, the net current is obtained

$$I = \int_{-\infty}^{\infty} dI_{1\to2} - dI_{2\to1} \propto A|T|^2 \int_{-\infty}^{\infty} N_1(E-eV)N_2(E)[f(E-eV)-f(E)]dE \quad (2.14)$$

If restricted only a few meV from the Fermi-level

$$N_1(E-eV) \simeq N_1(E) \simeq N_1(0) \text{ and } N_2(E) \simeq N_2(0)$$

then equation (2.14) may be formed as

$$\begin{aligned} I_{\text{nin}} &= A|T|^2 N_1(0)N_2(0) \textstyle\int_{-\infty}^{\infty}[f(E-eV)-f(E)]dE \\ &= A|T|^2 N_1(0)N_2(0)eV \equiv G_{\text{nin}}V \end{aligned} \quad (2.15)$$

where G_{nin} is a conductance. As a conclusion, current-voltage dependence of the junction can be find to be *ohmic* thus $1/G_{\text{nin}}$ can be denoted as tunneling resistance R_T.

2.1.4 NIS-tunneling

Next will be examined a case when the other electrode is a superconductor (NIS-junction). At thermal equilibrium at $T = 0$ all single-electron states in N-metal up to E_f are filled, whereas in S-metal there are single-electrons states only up to $E_\mathrm{f} - \Delta$ available. Without voltage source the Fermi-levels coincide and because of the energy-gap there is no tunneling current until $e|V| \geq \Delta$, in which case the current increases rapidly. When the voltage difference is increased the tunnelling electrons are faced with more unoccupied states and the current is further increased approaching NIN tunneling behaviour. Correspondingly, reversed polarity gives current only until $V \leq -\Delta/e$. The tunneling current can be calculated by replacing $N_2(0)$ in (2.15) with the superconducting density of states, keeping in mind that the zero energy level was chosen as the superconductor Fermi level so

$$I_\mathrm{nis} = A|T|^2 N_1(0) \int_{-\infty}^{\infty} N_{\mathrm{s}2}(E)[f(E - eV) - f(E)]dE. \tag{2.16}$$

Furthermore, if eguation (2.13) is substituded replacing $N_{\mathrm{s}2}$ then the current can be written as

$$\begin{aligned} I_\mathrm{nis} \quad &= A|T|^2 N_1(0) N_2(0) \textstyle\int_{-\infty}^{-\Delta} \frac{-E}{\sqrt{E^2-\Delta^2}}[f(E - eV) - f(E)]dE \\ &+A|T|^2 N_1(0) N_2(0) \textstyle\int_{\Delta}^{\infty} \frac{E}{\sqrt{E^2-\Delta^2}}[f(E - eV) - f(E)]dE. \end{aligned} \tag{2.17}$$

At $T = 0$ this can be simplified into the form

$$I_\mathrm{nis} = \begin{cases} G_{nin}\sqrt{V^2 - (\frac{\Delta}{e})^2} & (|V| > \frac{\Delta}{e}) \\ 0 & (|V| < \frac{\Delta}{e}) \end{cases} \tag{2.18}$$

An interesting observation is made when one consideres the differential conductance dI/dV. From (2.16) and (2.15)

$$G_\mathrm{nis} = \frac{dI_{nis}}{dV} = G_\mathrm{nin} \int_{-\infty}^{\infty} \frac{N_{2\mathrm{s}}(E)}{N_2(0)} \left[-\frac{\partial f(E + eV)}{\partial(eV)}\right] dE, \tag{2.19}$$

where $\left[-\frac{\partial f(E+eV)}{\partial(eV)}\right]$ represents a bell-shaped function with width kT. When $kT \to 0$ the conductance

$$G_\mathrm{nis} = G_\mathrm{nin} \frac{N_{2\mathrm{s}}(e|V|)}{N_2(0)} \tag{2.20}$$

directly measures the density of states. At finite temperature the differential conductance is smeared from the density of states as can be seen in figure (2.5). This smearing can be represented at zero bias voltage in a form [1]

$$\frac{G_{\rm nis}}{G_{\rm ns}}\Big|_{V=0} = \left(\frac{2\pi\Delta}{kT}\right)^{1/2} e^{-\frac{\Delta}{kT}} \tag{2.21}$$

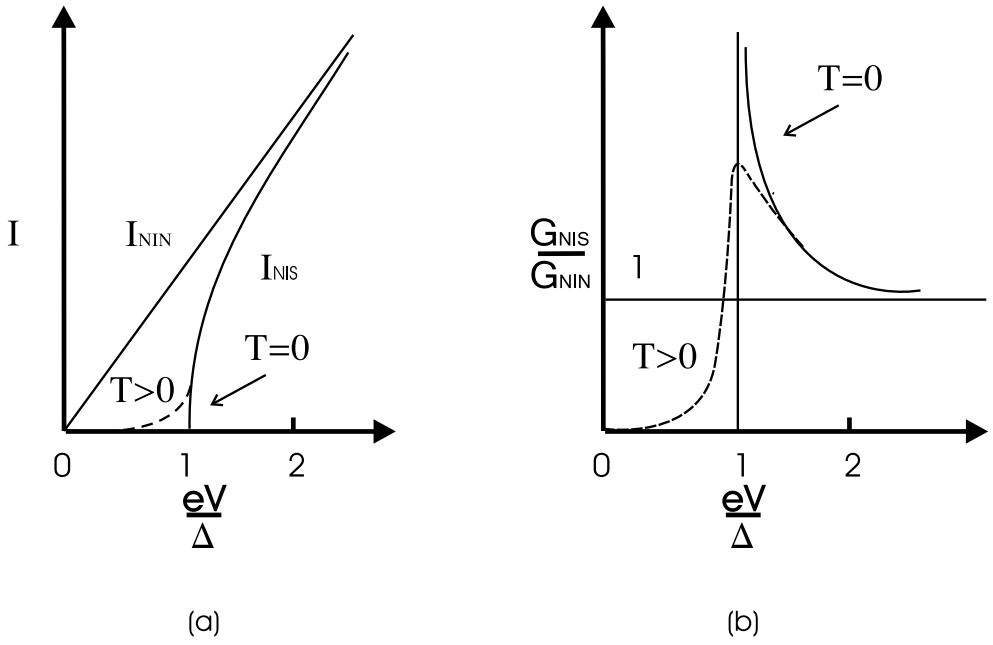

Figure 2.5: *Characteristics of normal metal-superconductor tunneling. (a) I-V curves of NIN and NIS junctions. (b) Ratio of the differential conductance G of the NIS and NIN junctions. Solid curves represent T=0 and dashed ones represent finite temperature.*

2.1.5 SIS-tunneling

If both metals are superconducting then the equation 2.14 becomes into the form

$$\begin{aligned} I_{\rm S_1IS_2} &= A|T|^2 \int_{-\infty}^{\infty} N_{\rm S_1}(E-eV) N_{\rm S_2}(E)[f(E-eV)-f(E)]dE \\ &= A|T|^2 N_1(0)N_2(0) \int_{-\infty}^{\infty} \frac{N_{\rm S_1}N_{\rm S_2}}{N_1(0)N_2(0)}[f(E-eV)-f(E)]dE \\ &= \frac{G_{\rm NIN}}{e} \int_{-\infty}^{\infty} \frac{|E-eV|}{\sqrt{(E-eV)^2-\Delta_1^2}} \frac{|E|}{\sqrt{E^2-\Delta_2^2}}[f(E-eV)-f(E)]dE \end{aligned} \tag{2.22}$$

In the final form the range of integration, when $|E| < |\Delta_2|$ or $|E-eV| < |\Delta_1|$, are excluded. That is, when the density of states is zero at the one or the other

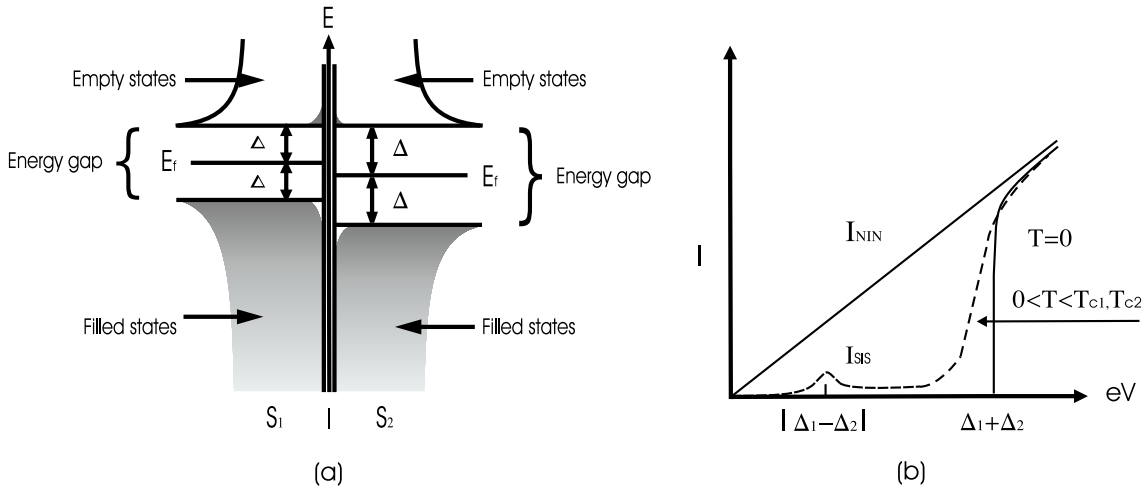

Figure 2.6: *(a) Energy level diagram with different gap values when* $V = (\Delta_1 - \Delta_2)/e$ *at finite temperature. (b) The negative resistance behaviour in current-voltage diagram, near* $eV = |\Delta_1 - \Delta_2|$

superconductor. At zero temperature all the energy levels are filled below the gap and there is no current until $V = (\Delta_1 + \Delta_2)/e$. At finite temperature the quasiparticles may occupy the states above the gap, leading to a current even at lower voltage differences. Especially, if superconductors have different gap values, as indicated qualitatively in fiqure (2.6), the current rises sharply when thermally excited quasiparticles are able to tunnel from above Δ_2 into the peaked density of available states above Δ_1 at $eV = \Delta_1 - \Delta_2$. When the voltage exceeds the value $\Delta_1 - \Delta_2$ the electrons are faced with the smaller density of states which leads into a smaller current until $V = (\Delta_1 + \Delta_2)/e$. The excistence of this "negative-resistance region" is sketched in figure 2.6(b).

2.1.6 Supercurrent

In 1962 B.D. Josephson proposed that a tunnel junction between superconductors, i.e., Josephson junction, should show a zero-voltage supercurrent due to the tunneling of condensed pairs, i.e., Cooper pairs [11]. The supercurrent is dependent on the phase difference of the macroscopic wavefunctions of the electrodes $\varphi \equiv \varphi_2 - \varphi_1$, i.e.,

$$I_S = I_C \sin(\varphi), \tag{2.23}$$

where I_C is a maximum of the supercurrent, i.e., the critical current. This is called a DC Josephson effect. In the AC Josephson effect, a Josephson junction will oscillate with a characteristic frequency which is proportional to the voltage across the junction so that

$$\hbar \frac{\partial \varphi}{\partial t} = 2eV. \tag{2.24}$$

Thus, if the voltage difference is applied over the junction the phase difference starts to evolve rapidly. Ideally, there is a dc-supercurrent only at zero voltage. The macroscopic pseudowavefunction, which describes all the Cooper pairs in a superconductor, was originally proposed by Ginsburg and Landau [12]. The pseudowavefunction $\psi(\vec{r})$ was introduced as a complex order parameter representing the local density of superconducting electrons $n_s(\vec{r}) \sim |\psi(\vec{r})|^2$. The paired electrons can be represented by a single wavefunction in the absence of current because all the pairs have the same phase - they are said to be "phase coherent". The form of the wavefunction is

$$\psi_i(\vec{r}) = |\psi_i(\vec{r})| e^{i\varphi_i(\vec{r})}. \tag{2.25}$$

Now quantum mechanical tunneling of Cooper pairs can occur at Josephson junction without breaking up the pairs by "locking together" the phases of the wavefunctions of different electrodes. The energy related to superconducting junctions, which couples the charging states together is called *Josephson energy* E_J. The supercurrent equation (2.23) can be calculated by substituting the macroscopic wavefunctions into ordinary quantum mechanical continuity equation. The appropriate energy function for the superconducting junction is the Gibbs *free* energy F. For small potential difference free energy is

$$F = \int V I_S dt = \int \frac{\hbar}{2e} \frac{d\varphi}{dt} I_C \sin(\varphi) dt = constant - \frac{\hbar I_C}{2e} \cos(\Delta\varphi).$$

If Josehson energy is marked as $E_J = \hbar I_C / 2e$ and the energy zero-level is chosen so that $constant = 0$. Then

$$H_J = -E_J \cos(\varphi) \tag{2.26}$$

is the Josephson coupling energy of the junction.

2.2 Josephson transistor

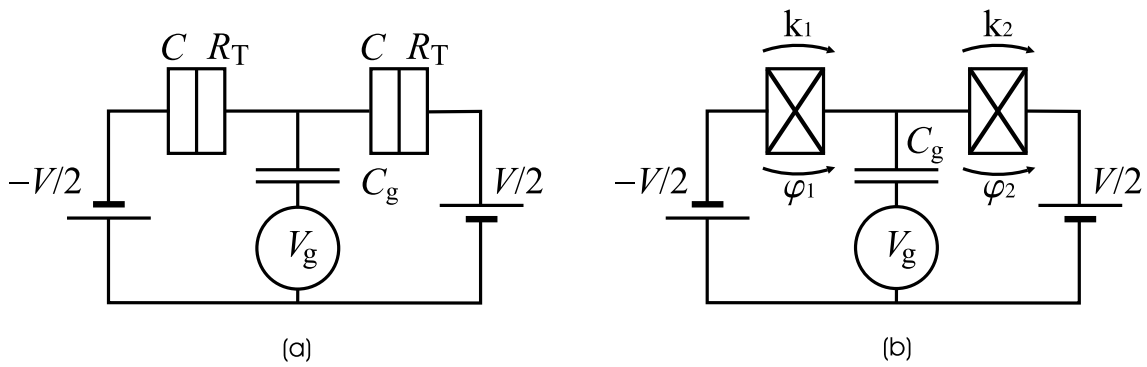

Figure 2.7: *(a) Single electron transistor where R_{T} denotes normal state resistance and C capacitance. (b) Superconducting Josephson transistor where φ denotes phase difference over the junction and k charge that has passed through the junction.*

The single-electron transistor (SET), device proposed by Averin and Likharev in 1986 [13] and first build by Fulton and Dolan [14] in the next year , consists of a small metallic island connected to the electrodes by two tunnel junction. The device is controlled through the voltage applied on a gate electrode capacitively coupled to the island. The Hamiltonian of a SET contains typically two parts: a tunneling Hamiltonian and a charging Hamiltonian. The first one can be either single-electron tunneling, if the SET is operated in the normal regime, or Josephson tunneling, in the case of a superconducting SET (Cooper-pair transistor or Josephson transistor). If concentrated on Josephson transistor the Hamiltonian of the transistor can be written as:

$$H = H_{\mathrm{C}} + H_{J1} + H_{J2}. \tag{2.27}$$

The first term $H_{\mathrm{C}} = E_{\mathrm{C}}(n - n_{\mathrm{g}})$ is the charging Hamiltonian in which $E_{\mathrm{C}} = (2e)^2/(2C_{\Sigma})$ denotes the electrostatic energy of a Cooper-pair on the island, n is the number of excess Cooper-pairs on the island and $n_{\mathrm{g}} = C_{\mathrm{g}}V_{\mathrm{g}}/2e$ is the charge induced by the gate voltage V_{g} on the gate capacitor C_{g} in units of $2e$. $C_{\Sigma} = C_1 + C_2 + C_{\mathrm{g}}$ is the total capacitance of the island. H_{J1} and H_{J2} are the Josephson coupling Hamiltonians of the two junctions

$$H_{\mathrm{J1}} = -E_{\mathrm{J1}} \cos(\varphi_1)$$

$$H_{\mathrm{J2}} = -E_{\mathrm{J2}} \cos(\varphi_2).$$

The total Hamiltonian should also contain a phenomenological quantity called "offset charge" which is believed [15] to originate partly from the differences in the work function of the electrodes and the island, and partly by the charge motion in the substrate. It is also assumed that the effect of the internal degrees of freedom (quasiparticles), and the electromagnetic environment is negligible.

2.2.1 Good quantum variables for the Josephson transistor

Equation of motion of the mechanical harmonic oscillator has a form:

$$m\frac{d^2x}{dt^2} + b\frac{dx}{dt} + kx = 0, \tag{2.28}$$

which can be written as:

$$\frac{d^2x}{dt^2} + 2B\frac{dx}{dt} + \omega_0^2 x = 0, \tag{2.29}$$

where $B := \frac{b}{2m}$ is a damping constant and $\omega_0 = \sqrt{k/m}$ is an angular frequency. Now, if considering an electric circuit, in which a resistance (R), an inductance (L) and a capacitance (C) are connected in series, then according to Kirchhoff:

$$\frac{d^2q}{dt^2} + \frac{R}{L}\frac{dq}{dt} + \frac{q}{CL} = 0, \tag{2.30}$$

which has the form of an equation (2.29). By analogy between mechanical and electrical system the Hamiltonians are

$$\begin{aligned} H_{\mathrm{mechanical}} &= \frac{p^2}{2m} + \frac{1}{2}kx^2 \\ H_{\mathrm{electrical}} &= \frac{1}{2}LI^2 + \frac{q^2}{2C} \end{aligned} \tag{2.31}$$

Furthermore, from the equation (2.24)

$$\varphi = \frac{2e}{\hbar}\int V dt = \frac{2e}{\hbar}LI,$$

and thus the current is

$$I = \frac{\varphi\hbar}{2eL},$$

which can be substituded into H_{C}. Then the Hamiltonian has the form

$$H_{\mathrm{C}} = \frac{1}{2L}\left(\frac{\hbar}{2e}\right)^2 \varphi^2 + \frac{q^2}{2C}. \tag{2.32}$$

Again, by analogy with the harmonic oscillator where the conjugated variables are p and k obeying commutation relation

$$[x, p] = i\hbar, \tag{2.33}$$

the charge q can be chosen to be a generalized coordinate corresponding to x. From the classical mechanics Lagrangian $L = T - U$ applied to equation 2.31 gives us generalized momentum

$$p = \frac{\partial L}{\partial \dot{q}} = LI.$$

Because operator $\varphi = \mathit{constant} \times LI$ the commutation relation can be proven to be as

$$[\hat{k}, \hat{\varphi}] = i, \tag{2.34}$$

where q is replaced with operator $\hat{k}$, which denotes charge that has passed through one junction in a Josephson transistor in the units of $2e$, as seen in figure (2.7). So far, the Josephson junction can be described by conjugated operators $\hat{\varphi}$ and $\hat{k}$, which have eigenstates $|k\rangle$ and $|\varphi\rangle$ so that

$$\begin{aligned} \hat{k}|k\rangle &= k|k\rangle \\ \hat{\varphi}|\varphi\rangle &= \varphi|\varphi\rangle \ . \end{aligned} \tag{2.35}$$

These are the variables for one junction. What is needed are the variables describing the electrostatic energy of the transistor. See figure (2.7)

- $n = k_1 - k_2$ = number of Cooper pairs on the island
- $k = (k_1 + k_2)/2$ = number of Cooper pairs that has passed the transistor
- $\varphi = \varphi_1 + \varphi_2$ = total phase difference over the transistor
- $\theta = (\varphi_1 - \varphi_2)/2$ = conjugate variable for n
- $n_{\mathrm{g}} = \frac{C_{\mathrm{g}} V_{\mathrm{g}}}{2e}$ = charge on the island induced by gate voltage V_{g}.

The variable θ was defined to get

$$[\hat{n}, \hat{\theta}] = i. \tag{2.36}$$

Since eigenstates of operators $\hat{k}$ and $\hat{\varphi}$ form a complete set, it can be formulated that

$$|k\rangle = \sum_{\varphi} |\varphi\rangle\langle\varphi|k\rangle \equiv \sum_{\varphi} \psi_k(\varphi)|\varphi\rangle. \tag{2.37}$$

Similarly

$$|n\rangle = \sum_{\theta} |\theta\rangle\langle\theta|n\rangle \equiv \sum_{\theta} \psi_n(\theta)|\theta\rangle. \tag{2.38}$$

And since

$$\psi_n(\theta) = \langle\theta|n\rangle = \frac{1}{\sqrt{2\pi}} e^{in\theta}, \tag{2.39}$$

one finally obtains

$$|n\rangle = \frac{1}{\sqrt{2\pi}} \int e^{i\theta n} |\theta\rangle d\theta, \tag{2.40}$$

which is the result that is needed to calculate the energy of the Josephson transistor at the charge basis $\{|n\rangle\}$.

2.2.2 Three-band model of the Josephson transistor

The simplest possible model to calculate the energy levels of the transistor is to take into account only two states $|n, \theta\rangle$ of lowest electrostatic energy [16]. However, the three-band model predicts an effective Josephson coupling about twice as large as the two-band model at $n_{\mathrm{g}} = 0$ [17]. Especially, in the case of niobium, large superconducting gap produces large coupling energy, $E_{\mathrm{j}} \simeq E_{\mathrm{C}}$ or even bigger, which makes the two-band approach too simplified. Total Hamiltonian when quasiparticles are excluded is

$$H = H_{\mathrm{C}} + H_{J1} + H_{J2}, \tag{2.41}$$

where

$$H_{Ji} = -E_{Ji} \cos\varphi_i. \tag{2.42}$$

With operator change

$$\begin{aligned} \hat{\varphi}_1 &= \tfrac{\hat{\varphi}}{2} + \hat{\theta} \\ \hat{\varphi}_2 &= \tfrac{\hat{\varphi}}{2} - \hat{\theta} \ , \end{aligned} \tag{2.43}$$

Hamiltonian goes into the form

$$H = E_C(n - n_\mathrm{g})^2 - (E_{J1} + E_{J2})\cos\frac{\varphi}{2}\cos\theta - (E_{J1} + E_{J2})\sin\frac{\varphi}{2}\sin\theta, \tag{2.44}$$

where $E_C = (2e)^2/2C_\Sigma$. The charging energy part in the matrix of the Hamiltonian is diagonal in the chosen $\{|n\rangle\}$ basis. In the calculation of the Josephson coupling, off-diagonal elements

$$\langle n'| - \sum_{\mathrm{i}=1}^{2} E_{\mathrm{J1}}\cos\varphi_\mathrm{i}|n\rangle, \tag{2.45}$$

change of basis is needed. Details of this calculation are presented in Appendix A. If $E_{\mathrm{J1}} = E_{\mathrm{J2}} \equiv E_\mathrm{J}$ then the off-diagonal matrix elements have simple form:

$$\langle n'|H_{J1} + H_{J2}|n\rangle = -E_J\cos(\frac{\varphi}{2})\delta_{n',n+1} - E_J\cos(\frac{\varphi}{2})\delta_{n',n-1}. \tag{2.46}$$

The matrix of the Hamiltonian in the $\{|n\rangle\}$ basis of the three states $|-1\rangle, |0\rangle$, and $|1\rangle$ is

$$H = \begin{pmatrix} E_\mathrm{C}(-1 - n_\mathrm{g})^2 & -E_\mathrm{J}\cos(\frac{\varphi}{2}) & 0 \\ -E_\mathrm{J}\cos(\frac{\varphi}{2}) & E_\mathrm{C}n_\mathrm{g}^2 & -E_\mathrm{J}\cos(\frac{\varphi}{2}) \\ 0 & -E_\mathrm{J}\cos(\frac{\varphi}{2}) & E_\mathrm{C}(1 - n_\mathrm{g})^2 \end{pmatrix}. \tag{2.47}$$

The secular equation is a polynomial of third degree:

$$(E - E_\mathrm{C}n_\mathrm{g}^2)(E - E_\mathrm{C}(1 - n_\mathrm{g})^2)(E - E_\mathrm{C}(-1 - n_\mathrm{g})^2) - E_\mathrm{j}^2(1 + \cos(\varphi)) = 0, \tag{2.48}$$

which is analytically solvable, even complicated. Solution is plotted in figure 2.8. The eigenenergies in a charge state basis forms periodic bands. The shape of the bands are dependent on the parameters n_g and φ with periocidy of 1 (scaled by 1/2e) and 2π, respectively. So far, the quasiparticles were ignored. In the next section this, and the benefits on using niobium will be considered qualitatively.

2.2.3 Niobium based Josephson junctions

A research of Coherent Cooper pair tunneling in nanoscale superconducting structures has been under an intensive study since these devices have been shown capable of operating as charge qubits [18, 19, 20, 21, 22] or building blocks for more complicated

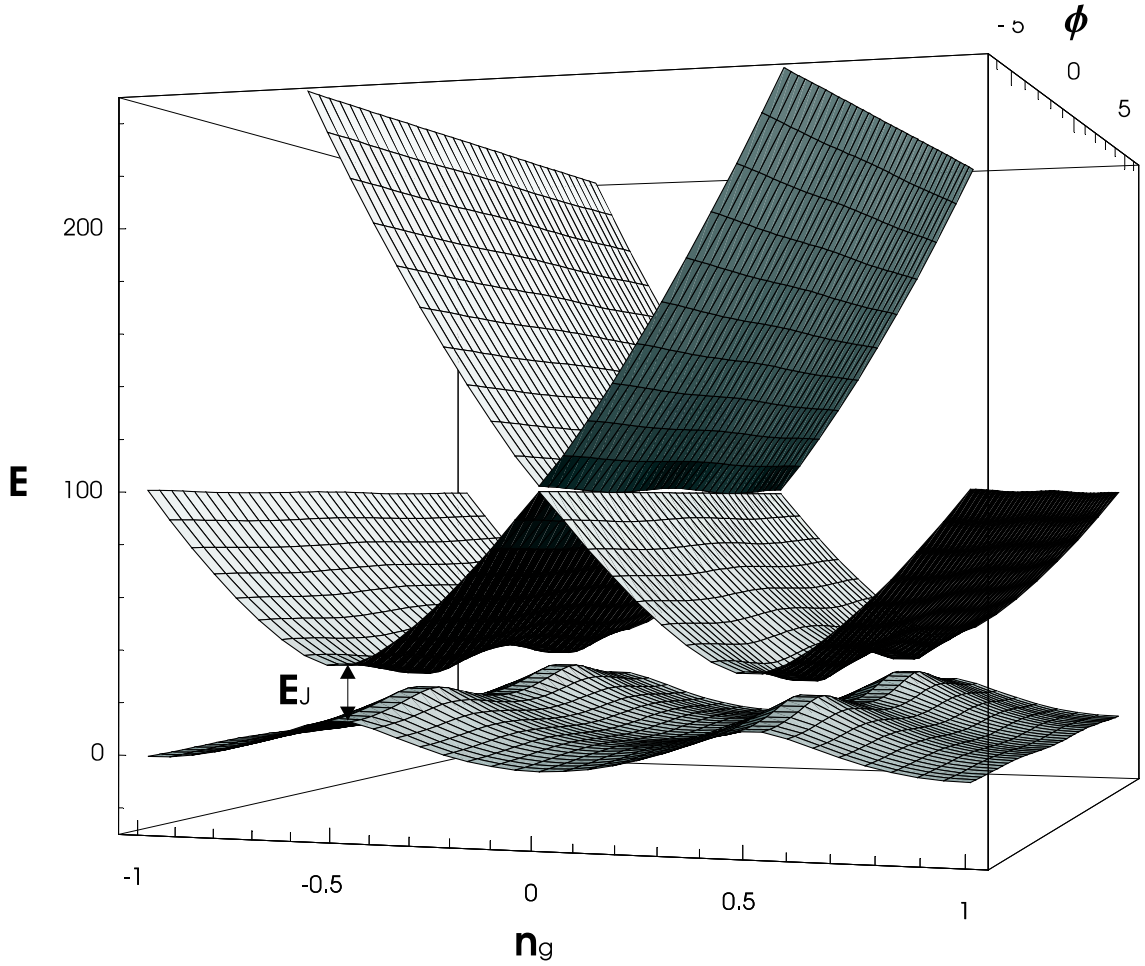

Figure 2.8: *Plot of the energy bands of the Josephson transistor as a function of total phase difference φ and gate induced charge n_{g}. Josephson coupling removes degeneracy forming energy gap. The Josephson coupling energy E_{J} equals the level spacing at the degeneracy point where $n_{\mathrm{g}} = \pm\frac{1}{2}$ and phase $\varphi = \pm 2\pi$. Here $E_J = 60\% E_{\mathrm{C}}$ and the energy scale is $100 \times E/E_{\mathrm{C}}$ $[\mu eV]$.*

devices[23, 24]. For example, suggestions to use a so-called Cooper pair pump to realise a metrological standard for current[25, 26] or measurement of a decoherence time [27, 28], have created a demand for high performance nanofabrication technigue. Niobium (Nb) would provide more reliable performance in many superconducting devices due to its large superconducting gap compared to aluminum (Al). The following table 2.1 shows differences between Nb and Al as construction materials for nano-devices. A theoretical calculation of the magnetic field dependence of the superconducting en-

Bulk properties/Material	**Aluminum**	**Niobium**
Critical temperature	1.175 K (0.1 meV)	9.26 K (0.8 meV)
Superconducting gap	2.07 K (0.18 meV)	16.33 K (1.4 meV)
Critical magnetic field	0.0105 T	0.2060 T

Table 2.1: *The difference between aluminum and niobium from the viewpoint of important key values.*

ergy gap, using the Ginzburg-Landau theory, agrees very well with measurements for aluminum [29]. This is important from the point of view of analysing measurements as can be seen later on. Also, much higher critical temperature of Nb produces much higher superconducting gap (2.5).

It is important to have high suppression of quasiparticles for the undisturbed manipulation of the cooper pairs. The parity effect (fig 2.9) sets the upper limit for the charging energy and the use of niobium would raise this limit much further due to its high Δ. At zero temperature with adiabatic gate modulation the system occupies the

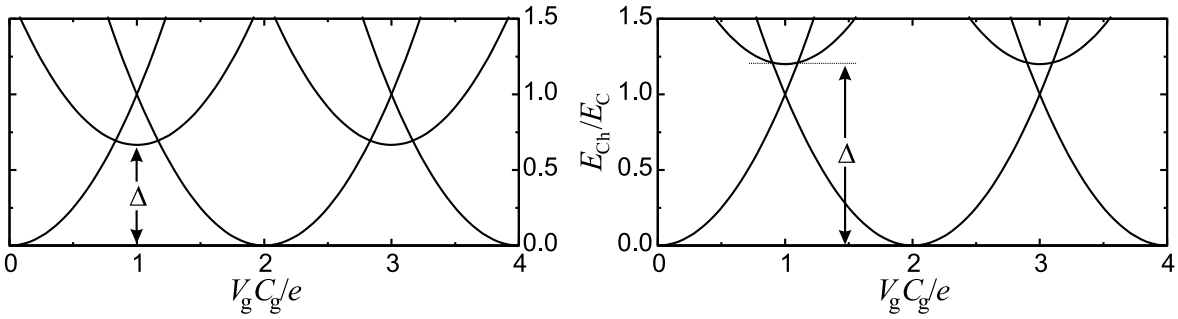

Figure 2.9: *Parabolas represent the electrostatic energy of the different configuration states of the transistor as a function of a gate charge. Here* $E_C = e^2/2C_\Sigma$ *and* $n_g = V_gC_g/e$. *At left side* $\Delta < E_C$ *at the degeneracy point. At right side* $\Delta > E_C$. *The minimum quasiparticle configuration energy, odd-n state, is* Δ.

lowest available energy state. In case of $\Delta < E_C$ it is favorable for a quasiparticle to enter the island in order for the system to be in its ground state. When $\Delta > E_{Ch}$ this entrance of a quasiparticle is suppressed. For heterostructure, Nb-Al junction, the

Josephson coupling energy is given by Ambegaogar-Baratoff formula for two different superconductors

$$E_{\mathrm{J}}^{Nb-Al} = \frac{R_{\mathrm{K}}}{2\pi R}\frac{\Delta_{\mathrm{Nb}}\cdot\Delta_{\mathrm{Al}}}{\Delta_{\mathrm{Nb}}+\Delta_{\mathrm{Al}}}\kappa\left(\frac{|\Delta_{\mathrm{Nb}}-\Delta_{\mathrm{Al}}|}{\Delta_{\mathrm{Nb}}+\Delta_{\mathrm{Al}}}\right), \tag{2.49}$$

where κ(x) is the complete elliptical integral of the first kind, $R_{\mathrm{K}} = h/e^2 \simeq 25k\Omega$ and R is the normal state tunneling resistance. Since Δ_{Nb} is an order of magnitude larger than Δ_{Al} producing high $E_{\mathrm{J}}^{\mathrm{Nb-Al}}$ and tolerating better any additional sources of energy, it is possible to have both the high charging energy and the Josephson energy, and still high normal state resistance of the junction R_{t}. At finite temperatures things are more complicated, because the equilibrium probability of odd or even occupation of the island is governed by the odd-even free energy difference of the island [31].

Chapter 3

Sample fabrication

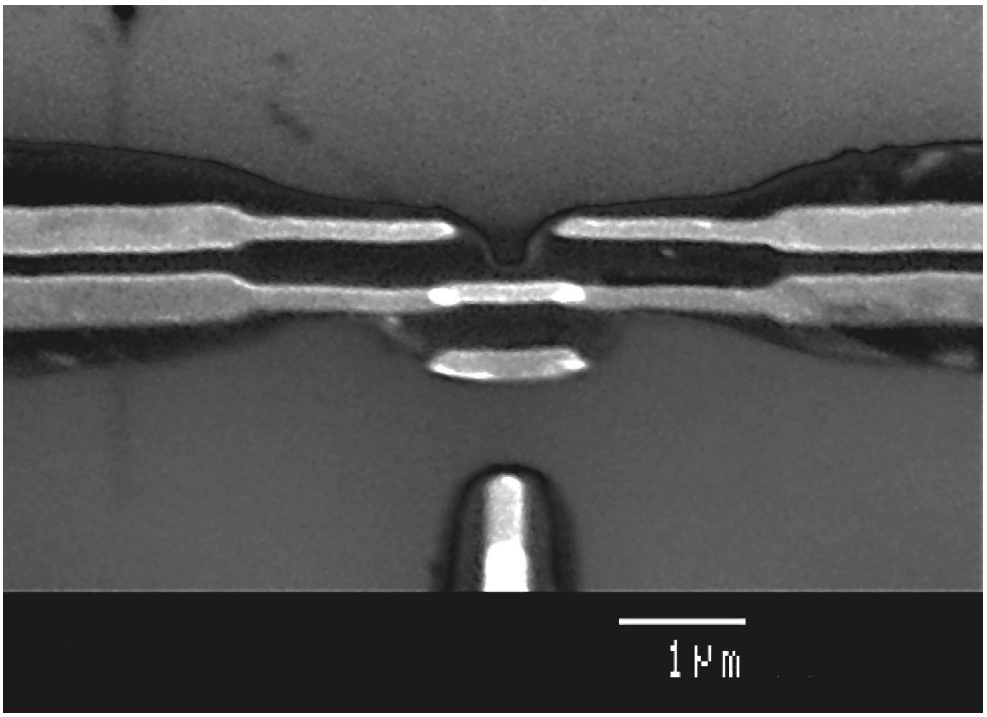

Figure 3.1: *Scanning electron microscope (SEM) image of the Al-AlOx-Nb-AlOx-Al transistor. Brighter lines are niobium and darker aluminum. Vertical line below is the gate voltage conductor. White spots* $1\mu m$ *apart are the tunnel junctions.*

Electron beam lithography enables fabrication of extremely fine patterns. It has become possible to fabricate metallic tunnel junctions in a controlled way with capacitances in the range of C = 10^{-15}F. In this case the charging energy associated

with a single-electron charge, $E_C \equiv e^2/2C$, is of the order of $10^{-4}eV$, which corresponds to a temperature scale $E_C/k_B \simeq 1K$. In this work, good quality submicron Nb/AlOx/Al single tunnel junctions and single electron transistors (SET) with Nb island and Al electrodes were fabricated using the conventional self aligning shadow evaporation technique with oxidation between to form AlOx (see fig. **??**). The nanostructure fabrication consists of several steps starting from the oxidation of the silicon substrate, covering it with electron sensitive material, patterning by SEM, metal evaporation and finally the lift-off. The final product is a mixture of knowledge, skill and good quesses. Despite of reports claiming that it is not possible to fabricate high quality Nb-based superconducting single-electron devices, recipe of fabrication will be shown. The results were obtained with the standard e-beam lithography process followed by a slightly different procedure and recipe.

3.1 Preparation of the sample

Samples were fabricated on a heavily oxidized Si substrate. A thickness of thermal $SiO_2 \simeq 375$ nm was achieved by oxidazing the p-type boron-doped wafer for 6 h at 1100 °C at steady oxygen flow which is slightly more than usual recipe. Based on a phenomenological observation thicker SiO_2 layer gives larger undercut profile due to the electrons bouncing from the surface of the SiO_2 while patterning with e-beam. When the primary electrons hit from the substrate their energy is dissipated in the form of secondary electrons with energies 2 to 50 eV. These electrons are mainly responsible for the undercut profile (see figure 3.4). A small part of the secondary electrons have energy of order of 1 keV which has an effect on widening the pattern of the mask. As the electrons penetrate through the resist into the substrate, part of them return back causing additional exposure of the resist. A lift-off mask with large undercut profile is essential for the fabrication, ensuring the removement of remnants of the resist, therefore reducing the suspected outgassing during the evaporation. The large undercut is achieved by reducing the voltage used in e-beam but it also has an effect of widening the pattern.

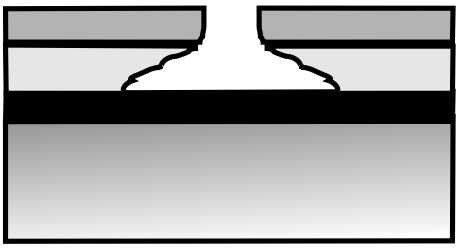

Figure 3.2: *Undercut profile. From the bottom: silicon, SiO_2, resist 1, resist 2.*

3.2 Resists

After the oxidation, SiO_2 surfaces were cleaned with acetone and isopropanol. Then polymethylmethacrylate (PMMA) and co-polymer [P(MMA-MAA)] were spun on the silicon chips.

Layer	Resist	Solvent	Spinning speed [rpm]	Baking time at 160 ℃ [min]
1.	9% PMMA-MAA	acetic acid	4000	45
2.	3% PMMA	chloro benzene	3000	60

Table 3.1: *Parameters for spinning the resist layers.*

The spinning rates for PMMA and P(MMA-MAA) were 3000 and 4000 rpm, respectively and the spinning time was 30 s for both. This also differs from the usual recipe which is 3000 and 6000 rpm. That way the thickness of the PMMA and P(MMA-MAA) were approximately 250 nm and 350 nm, respectively. Thicker bottom layer was supposed to protect the upper layer from electrons scattering from the surface thus enabling bigger current dose and hence cleaner surface. The resists were baked at 160 °C 45 min for the bottom layer and 60 min for the upper layer.

3.3 Dose determination

Determining the correct dose for a pattern is complicated because in addition to the primary and secondary electrons, the backscattering electrons should also be included.

These electrons have a significant range, depending on the substrate, voltage and the resist used. The range may be several micrometers. A higher beam energy (voltage) causes deeper penetration into the substrate and fewer secondary electrons reach the surface. This means smaller undercut profile. On the other hand, smaller energy demands higher current, which limites accuracy. The dose also depends strongly on success of focusing of the beam. Also, dose determination between different models of SEM's are not directly proportional. Furthermore, the dose needed varies weekly even at the same SEM. However, the relation of the doses between different part of the pattern is comparable. The Nb-based samples were mainly done using scanning electron microscope JEOL JSM840 A, with acceleration voltage 20kV. A DesignCad 2D-program was used for pattern design, and NPGS-program for patterning. The following table 3.2 shows relative differences between the doses for aluminum based, and niobium based samples. The colour codes are shown in figure (3.3).

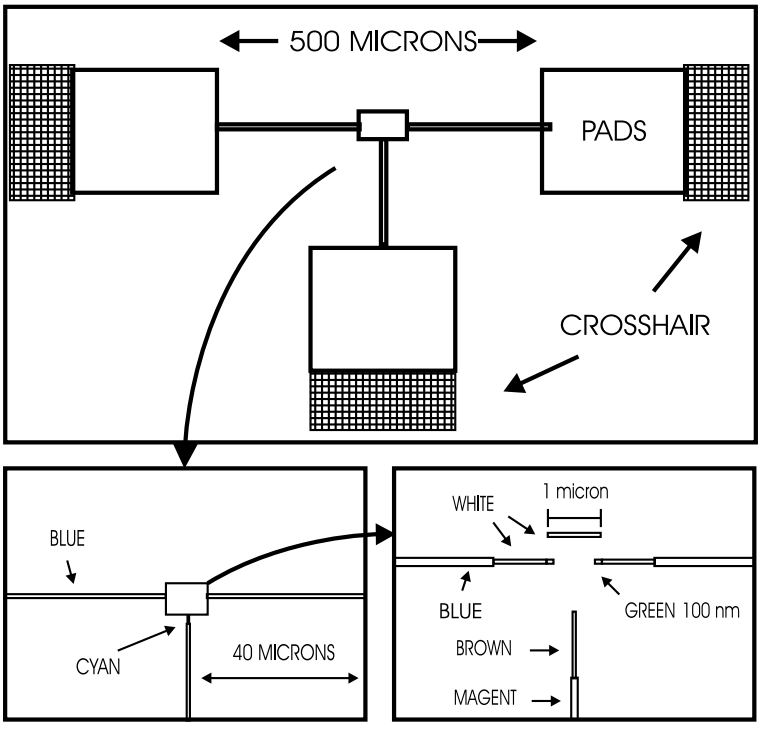

Figure 3.3: *Design of the transistor. The dose for each layer is specified in table 3.2.*

After the patterning the samples were developed. See table (3.3) To develop the upper layer of the PMMA resist the sample was immersed in a mixed (1 : 2) solution

COLOUR	WHITE	RED	GREEN	BLUE	BROWN	CYAN	MAGENT
LINE WIDTH [µm]	0.050	0.200	0.050	0.100	0.050	2.000	0.050
LINE DOSE [nC/cm]	2.0	1.5	1.7	4.0	1.6	0.9	2.5
MAGNIFICATION	1000	1000	1000	1000	1000	1000	1000
CENTER-TO-CENTER DISTANCE [Å]	123.6	123.6	123.6	123.6	123.6	123.6	123.6
LINE SPACING [Å]	123.6	123.6	123.6	123.6	123.6	123.6	123.6
COARSE BEAM CURRENT [A]	$3*10^{-11}$	$3*10^{-11}$	$3*10^{-11}$	$3*10^{-11}$	$3*10^{-11}$	$3*10^{-11}$	$3*10^{-11}$
MEASURED CURRENT [pA]	9.8	9.8	9.8	9.8	9.8	9.8	9.8
VOLTAGE [kV]	20	20	20	20	20	20	20

COLOUR	BLUE CROSSHAIR	PADS
LINE WIDTH [µm]	5.000	AREA
LINE DOSE [nC/cm]	4.0	-
AREA DOSE [µC/cm^2]	-	600
MAGNIFICATION	19	19
CENTER-TO-CENTER DISTANCE [Å]	5059.6	20238.3
LINE SPACING [Å]	5059.6	20238.3
COARSE BEAM CURRENT [Å]	$1*10^{-6}$	$1*10^{-6}$
MEASURED CURRENT [nA]	8.6	57
VOLTAGE [kV]	20	20
MAXIMIZED CURRENT [nA]	62	62

COLOUR	WHITE	RED	GREEN	BLUE	BROWN	CYAN
LINE WIDTH [µm]	0.050	0.20000	0.050	0.100	0.050	2.000
LINE DOSE [nC/cm]	3.75	3.85	3.95	5.2	3.45	2.4
MAGNIFICATION	1000	1000	1000	1000	1000	1000
CENTER-TO-CENTER DISTANCE [Å]	123.6	123.6	123.6	123.6	123.6	123.6
LINE SPACING [Å]	123.6	123.6	123.6	123.6	123.6	123.6
COARSE BEAM CURRENT [A]	$1*10^{-11}$	$1*10^{-11}$	$1*10^{-11}$	$1*10^{-11}$	$1*10^{-11}$	$1*10^{-11}$
MEASURED CURRENT [pA]	4.4	4.4	4.4	4.4	4.4	4.4
VOLTAGE [kV]	20	20	20	20	20	20

COLOUR	BLUE CROSSHAIR	PADS
LINE WIDTH [µm]	5.000	AREA
LINE DOSE [nC/cm]	4.0	-
AREA DOSE [µC/cm^2]	-	600
MAGNIFICATION	19	19
CENTER-TO-CENTER DISTANCE [Å]	5059.6	20238.3
LINE SPACING [Å]	5059.6	20238.3
COARSE BEAM CURRENT [Å]	$1*10^{-6}$	$1*10^{-6}$
MEASURED CURRENT [nA]	5.0	47
VOLTAGE [kV]	20	20
MAXIMIZED CURRENT [nA]	59	59

Table 3.2: *Table for successful patterning. Upper table is for the Niobium sample and below one for aluminum with similar design. The maximum current should always be adjusted at the same value between the different patterning set.*

Developer	Time [s]
MIBK (methyl-iso-butylketon) : Isopropanol 1 : 2	38
Methylglycol : Methanol 1 : 2	8

Table 3.3: *Developers and developing times used. Mibk/Isopropanol mixture is for upper resist and Methylglygol/Methanol for lower the resist.*

of methyl-iso-butylketon (MIBK) and isopropylic alcohol for 30 s. The lower layer P(MMA-MAA) was developed in a mixture of (1 : 2) methylglycol and methanol for 8 s. Between the developers the sample was rinsed in an usual way in isopropylic alcohol but after the second developer the rinse was placed in an ultra sonic machine (FinnSonic). Before evaporation the uncovered SiO_2 surfaces were cleaned in a reactive ion etcher (AXIC BENCHMARK) for 30 s at 30 mTorr pressure with 50 sccm flow of oxygen and 48 W RF-power. After the etching the mask was baked below 90 °C for 30 min to get rid of the moisture and to glaze the mask to endure the heating by the niobium at the evaporation.

3.4 Evaporation

The evaporation took place in an ultrahigh vacuum (UHV) chamber equipped with a cryo-vacuum pump (Cryo-Torr High vacuum pump, CTI-Cryogenics) and a liquid-nitrogen trap (see fig. 3.5). The pressure was $2 - 4 \times 10^{-8}$ during the evaporation. The evaporation rate for Al and Nb was 0.5 nm/s and 0.75 nm/s, and the power of the electron gun was 0.35 kW and 2.0 kW, respectively. In addition to be able to form the tunnelling barrier by oxidising aluminium, the order of evaporation has another meaning. When the aluminum leads are evaporated first, extra metal sticked at the top of the stencil mask serves as a protective layer for the resist while evaporating the niobium. The next step was to let the aluminum cool down for 5 minutes to ensure the hardness and stability of the aluminum. Then the process continued by oxidating the

sample at steady flow of oxygen, pressure being 16 mBar for three minutes. The layer thicknesses were chosen to be 40 nm for the Al and 60 nm for the Nb. The resulting linewidth was 125 nm. After evaporation of the niobium (99.9%, Goodfellow) the sample was let to cool down again followed by oxidation at athmospheric pressure for 3 minutes. The process was completed by lift-off by placing the sample in an acetone and slowly heating to a boiling point of 56 °C and leaving there for three hours. Finally the sample was cleaned by reactive ion etcher with the parameters shown before.

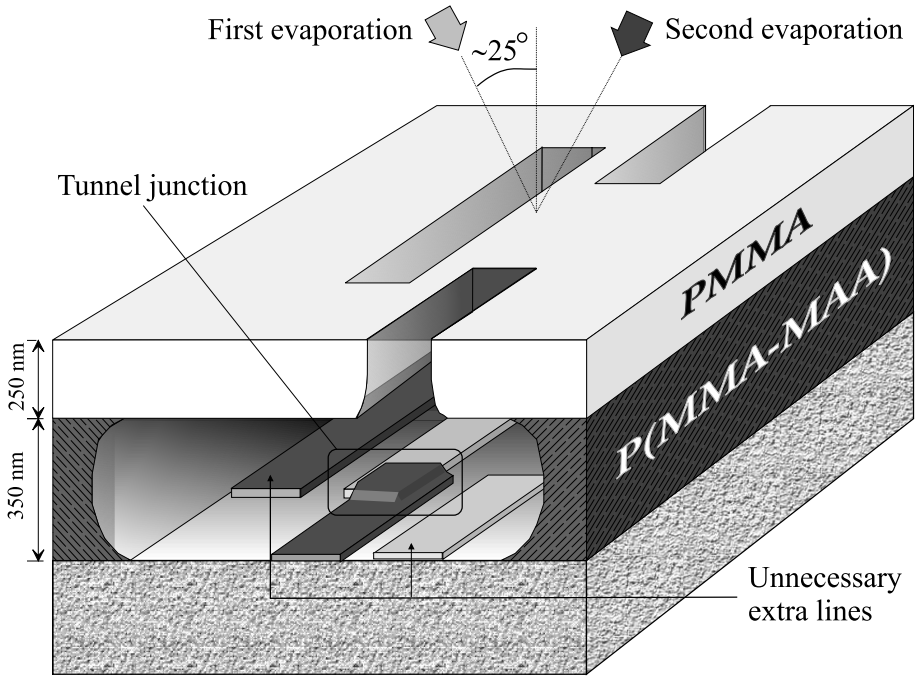

Figure 3.4: *Principle of the self-aligning technigue. The tunnel junction is formed between the two metallic layers which are evaporated at different angles so that the result is an overlapping structure. The tunnel barrier is formed by oxidising the first layer before evaporating the second one. The first layer is usually Al thus the barrier is formed of* AlO_x.

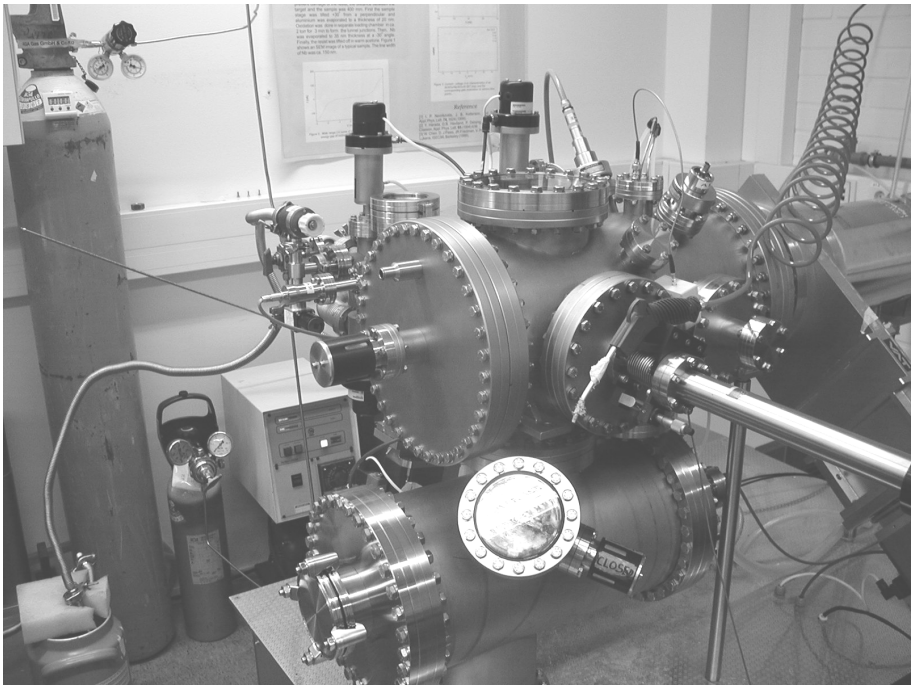

Figure 3.5: *Photograph of the ultrahigh vacuum (UHV) chamber equipped evaporator. As a speciality, it has a long distance (40 cm) between the source metal and the sample state. This may have an effect on the Niobium samples since the power needed to evaporate Nb exceeds 2 kW, and thus the long distance reduces the effect of the heat radiation on the sample. And as an accessory it is equipped with a cold trap between the oxidation chamber and the oxygen flow pump (left down in a picture).*

Chapter 4

Measurements

The measured quantities in these experiments were the tunneling conductance and the tunneling current as a function of voltages, temperature and/or an applied magnetic field. All the sub-Kelvin measurements were done in a small dilution refrigerator (Nanoway, PDR50) placed inside an electrically shielded room (Euroshield). Current and voltage measurements were done with DL-Instrument's 1211 current amplifier and 1201 low-noise pre-amplifier. All the wires in refrigerator contained commercial π-filters at room temperature and at 4.2 K. Between the filters manganin wires inside CuNi tube (electric shielding) were used to reduce a heat leak. In addition, home made strip filters were fabricated and mounted into the lines at the sample stage. The temperature in dilution refrgerator was measured using a resistance bridge (Picowatt AVS-47) and a carbon resistor which was originally calibrated using primary Coulomb blockade thermometer (Nanoway CBT). In critical temperature measurement of a niobium a commercial calibrated Cernox resistor was used. Magnetic field measurements were carried out in a superconducting Nb-Ti wired magnet (Cryomagnetic Systems, OXFORD INSTRUMENTS). The power supply for the magnet was 6260B (Hewlett Packard). Measurement set up using lock-in amplifier is shown in figure 4.1.

In the measurements bias voltage was obtained from the battery powered voltage source slowly sweeping the output voltage between ± 4 V DC. Also, the excitation, i.e., AC-voltage with amplitude dV for lock-in measurement was obtained from the same box. The alternating reference signal dV ($\approx$ 0.1 mV and 87.5 Hz) and bias voltage

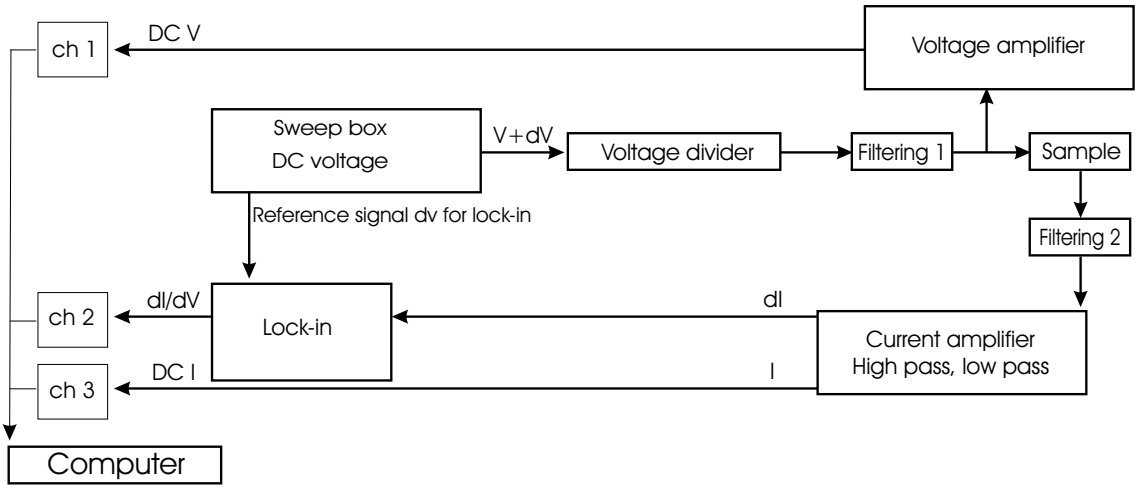

Figure 4.1: Schematic measurement setup using the lock-in amplifier.

V was fed into commercial π-filter via voltage divider. Thus, the voltage regime over the sample was ± 15 mV and the excitation (reference signal) ≈ 0.7 μV. After the sample the signal was filtered again with π-filter and fed into the current amplifier, which picked and amplified the DC signal into the computer via ch 3, and directed the AC component into the lock-in amplifier. The lock-in amplifier picked the signal at the reference frequency and thus fed out dynamical conductance dI/dV to ch 2. Meanwhile, voltage amplifier picked DC component between the first filtering and the sample and, amplified it and fed into the computer via ch 1. Between the channels 1-3 (inside the shielded room) and the computer (outside) the signals had to go through the highly efficient low pass filters (Euroshield) mounted in the wall of shielded room.

4.1 Critical temperature $T_{\mathrm{c}}^{\mathrm{Nb}}$

A method of determining $T_{\mathrm{c}}^{\mathrm{Nb}}$ is shown in figures 4.3 and 4.4. While measuring the zero bias conductance the samples were gradually heated over the critical temperature of niobium until the weaker temperature dependence of Coulomb blockade became visible after the vanishion of $\Delta_{\mathrm{Nb}}(T)$. The samples were heated using ohmic resistor and measured with commercial calibrated Cernox resistor. The set up is shown in figure 4.2. The values for $T_{\mathrm{c}}^{\mathrm{Nb}}$ were obtained from the conductance measurement (see

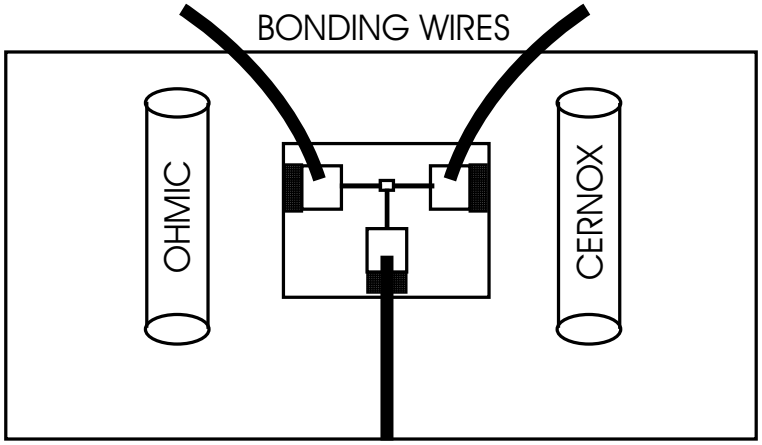

Figure 4.2: T_c^{Nb} measurement set up. The sample is clued on a copper plate with commercial calibrated Cernox resistor on the right and a thermal resistor for heating on the left. The distance between the Cernox and the resistor is ≈ 2 cm.

fiqure 4.4). The critical temperature obtained for the best sample was 8.5 $\pm$ 0.5 K, which is very close to $T_c^{Nb} = 9.3$ K in bulk Nb. It may be possible that the reduction of the T_c^{Nb} from the bulk value is not caused by impurities in the sample due to the fabrication process but the dimensions of the sample [8]. The second critical field $H_{C,2}^{Nb}$ was determined similarly as a function of a magnetic field.

4.2 Charging energy

The charging energies of the samples were derived from the normal state conductance curve measured at 4.2 K with magnetic field of $B \sim 5$ T. See figure 4.5. Undesired background effect becomes observable at high bias voltages due to distortion of the potential barrier. In this case it was distruptive already at low bias voltage due to the small work function of Niobium. The effect of the background was subtracted by the lines parallel to asymtotes. The $\Delta G/G_T$ (see eq. 4.1) was set to correspond to the difference between the crossing point of the lines and the lowest value of the conductance curve. The charging energies of the samples 3-5 (see table 4.1) were also obtained from the V_G modulated $I-V$ curve at temperatures around 100 mK without magnetic field. Obtained charging energies varied between $E_C \approx 68 - 156$ μeV. The

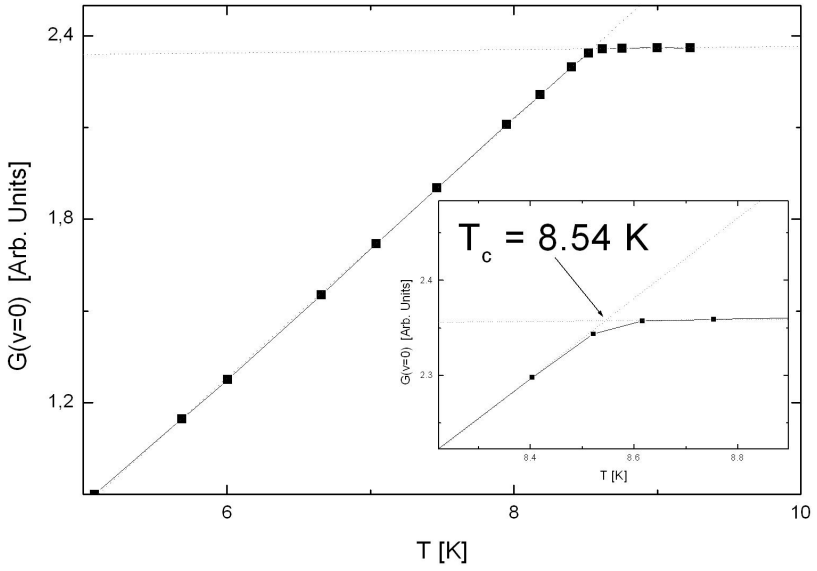

Figure 4.3: A method for determining the critical temperature T_c^{Nb}. Circles are the zero bias conductances obtained from the dI/dV measurement. (See figure 4.4).

charging energies were calculated from the equation

$$\Delta G/G_T = \frac{E_C}{6k_B T}, \tag{4.1}$$

which neglects the effects due to electromagnetic environment.

4.3 Characteristics of the samples

Sample	R (T_{room}) [kΩ]	R (4.2 K) [kΩ]	E_C [μeV]	H_C^{Nb} [T]	Δ_{Nb} [meV]	T_C^{Nb} meas [K]	E_J [μeV]	E_C [μeV]
1	55	70	78	3.1	1.93	7.81	41	-
2	21	30	40	2.65	1.92	8.1	95	-
3	-	31	36	3.5-4.5	1.45	8.54	92	28.5
4	27	32	38	-	2.29	-	89	34
5	20	23	34	2.45	1.9	-	123	31.5

Table 4.1: Characteristic of the samples. See text.

All the parameters from the samples measured are shown in table 4.1. The T_c^{Nb} of

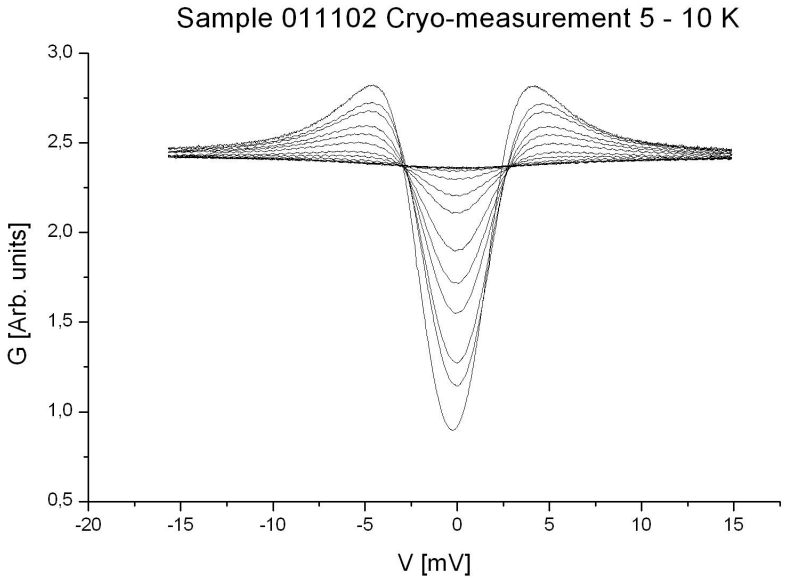

Figure 4.4: Conductance measurement. Curves were obtained by gradually heating the sample over the critical temperature T_c^{Nb}. One curve represents one sweep over the bias voltage regime at constant temperature.

the samples 4 and 5 were probably higher than notified in table 4.1. The measurements were interrupted due to technical problem. The resistances in 2nd and 3rd column were measured at room temperature and in liquid He at 4.2 K, respectively. The gap values Δ_{Nb} in 6th column were measured at 4.2 K, and are unrealistic high due to measurement set up corresponding to NISIN measurement, except the 3rd sample which was measured at 150 mK (SISIS). The Josephson coupling energies were obtained from the Ambegaogar-Baratoff -formula for two different superconductors (see eq. 2.49), which yielded $E_{\mathrm{J}} \approx 41 - 123\ \mu$eV. Thus the ratio $E_{\mathrm{J}}/E_{\mathrm{C}}$ varied between 0.26 and 1.81. The charging energies in 4th column were obtained at 4.2 K with magnetic field 5T and backround subtracted as explained before, and the charging energies in 10th column were obtained from the period of the gate modulated $I - V$ at base temperature 100 mK.

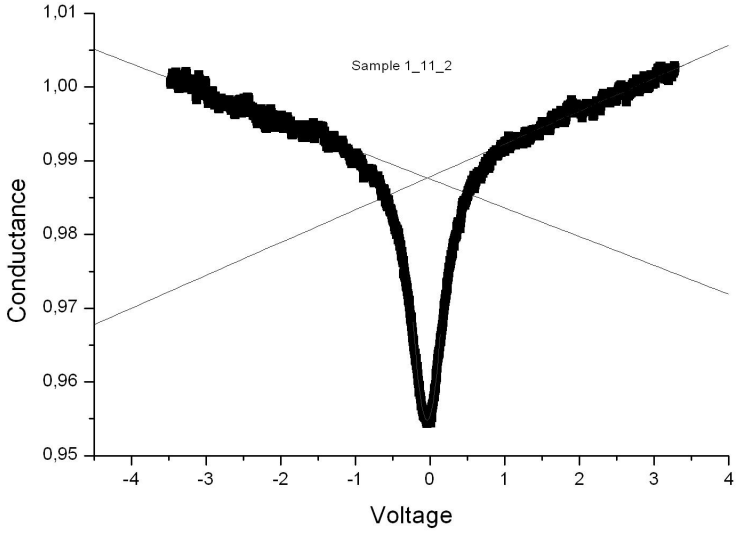

Figure 4.5: The charging energy measurement at 4.2 K with magnetic field $5T \gtrsim H_{\mathrm{C},2}^{\mathrm{Nb}}$. Conductance as a function of bias voltage. The height of the conductance dip was measured from the crossing point of the lines parallel to asymtotics.

Chapter 5

Subgap transport phenomena

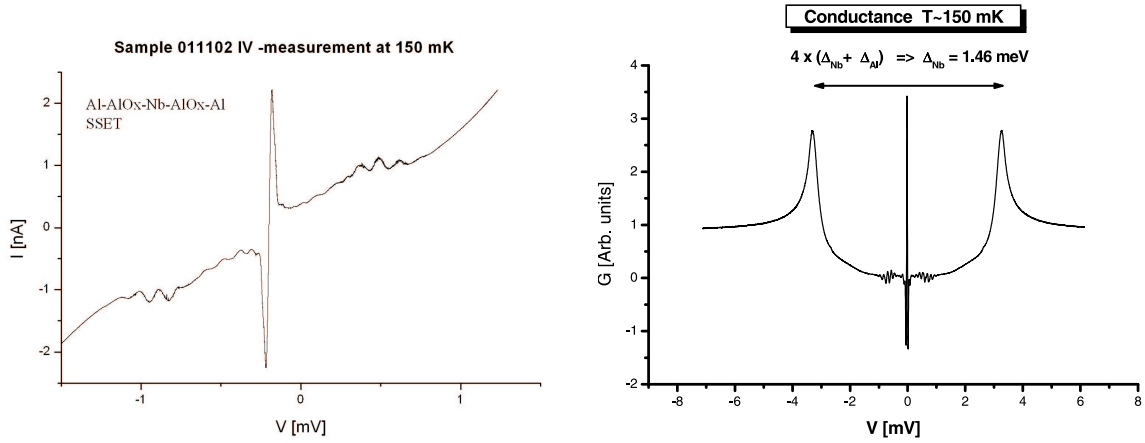

Figure 5.1: Left: I-V curve from the sample number 3 in table 4.1. Right: Conductance showing high gap value and regularly spaced oscillation below $V \lesssim 0.9$ mV.

In Fig. 5.1 (left) I-V characteristics and (right) a dI/dV-curve are shown for one of the samples with $E_{\mathrm{C}} \sim 34$ μeV and $E_{\mathrm{J}} \approx 92$ μeV. The gap with a width of $4(\Delta_{\mathrm{Al}} + \Delta_{\mathrm{Nb}})/e$ is clearly visible and the maximums in the dI/dV-curve yield $\Delta_{\mathrm{Nb}} \approx$ 1.45 meV. Here it is assumed $\Delta_{\mathrm{Al}} \approx 0.2$ meV. The oscillations seen in the dI/dV-curve near the supercurrent at $V = 0$ are clearly visible in three of the measured samples. These peaks at the bias voltages below $V \lesssim 0.9$ mV are equally spaced in V and appear only when decreased magnetic field below the critical of aluminum $H_{\mathrm{c}}^{\mathrm{Al}}$, i.e., in SISIS configuration. It has been verified that the positions of these peaks do not depend on the applied magnetic field (fig. 5.2). Also these resonances cannot be

due to the coupling of the Josephson oscillations to the electromagnetic environment of the sample. To rule out this hypothesis, Al-only single junctions and SET's with the same SEM design for the contact pattern were fabricated, and measured with the same dilution refrigerator. The subgap conductances of these samples can be regarded as a spectral analysis of the environment, as seen by the sample. The result was that mild resonances do exist but only below 0.15 meV. Above this value (and up to the quasiparticle threshold voltage) the I-V's and the conductivities were exactly flat, for all the samples measured. The observed resonance pattern is similar to so-called Josephson-quasiparticle -cycle (JQP), which, however, appears only at much larger voltages, $\Delta_{\mathrm{Nb}} + \Delta_{\mathrm{Al}} + E_{\mathrm{C}} \leq eV \leq \Delta_{\mathrm{Nb}} + \Delta_{\mathrm{Al}} + 3E_{\mathrm{C}}$, which in the sample yields 1.72 $eV \lesssim eV \lesssim$ 1.87 eV.

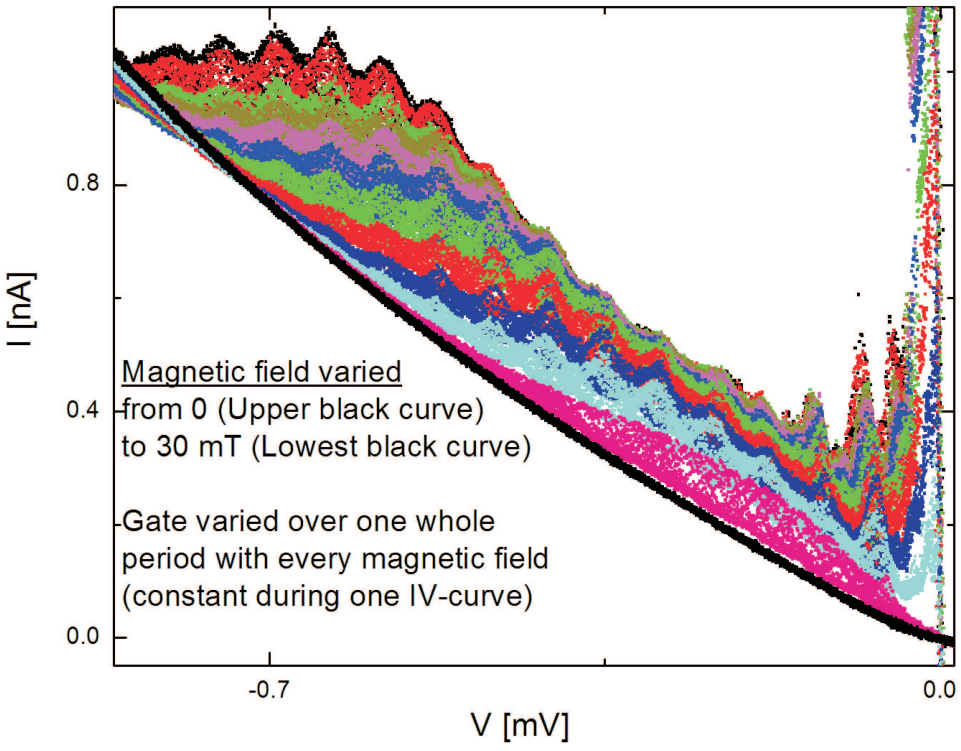

Figure 5.2: I-V characteristics measured with different gate voltages V_{g} and magnetic fields ranging: From the uppest $H = 0$, to the lowest $H = 30$ mT curve. Different colours correspond to different value of magnetic field. See text.

Figure (5.2) shows the oscillations near supercurrent. The plot includes all data

from the measurement below 0.9 mV. Each colour indicates constant magnetig field while bias voltage V_b and gate voltage V_g were varied. First, the bias voltage was set to a certain value, then the gate voltage was varied over the whole period. The bias voltage was set to another value, and again varied with the gate voltage until the whole bias measurement range from -15 mV to 15 mV was completed. As seen, the position of the peaks do not depend on the applied external magnetic field or the gap of the aluminum electrodes, but the baseline of the I-V curve shows clear dependence on the magnetic field. It appears that measured Al/AlO_x/Nb/AlO_x/Al show clear signature of the resonant tunneling of Cooper pair combined with the elastic cotunneling of quasiparticles, q-MQT, through the barrier of Δ_{Nb} [51].

5.1 Resonant tunneling of Cooper pairs

If considering the simplest and the most probable resonant tunnelling event, seen in Fig. 5.3, where one Cooper pair tunnels into the island, the constraint is obtained as

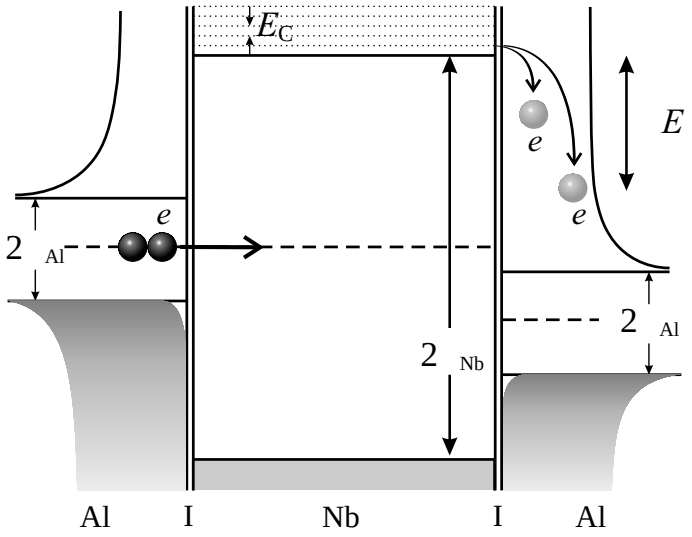

Figure 5.3: The resonance tunneling. Cooper pair enters the island. This 2e excess charge has to be carried out into the external circuit which is inelastic process. The rate of the process is determined by the electromagnetic environment, which ability to absorb energy is described by the probability function P(E) from the 'P(E)' theory [52]. ΔE is the energy difference from above the Nb gap into single electron state.

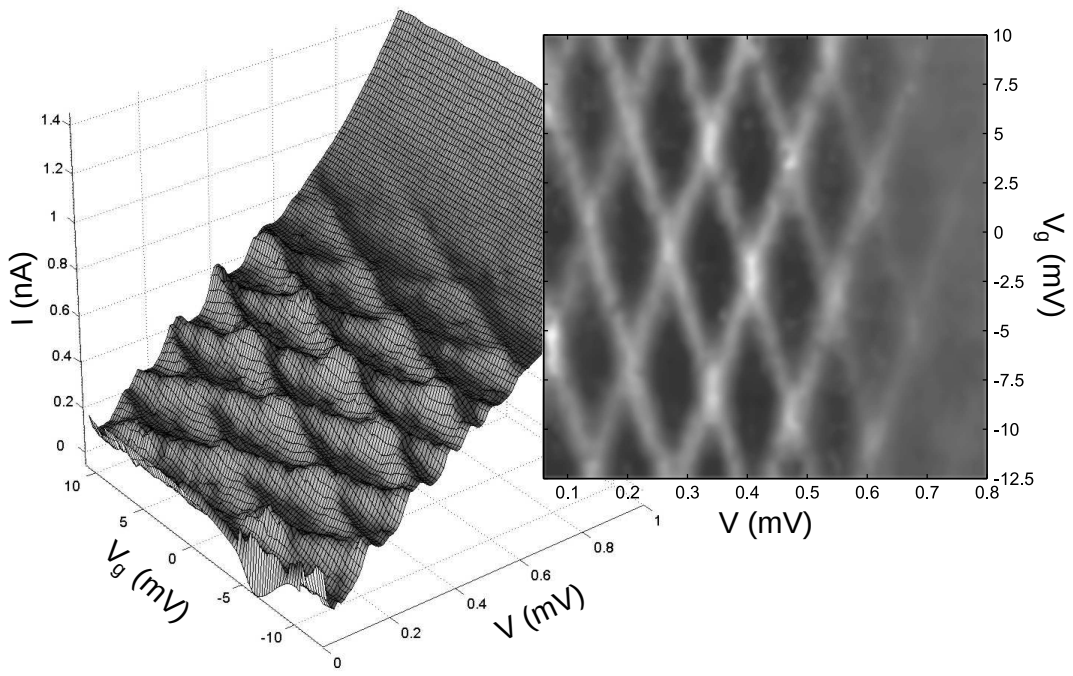

Figure 5.4: Left: The peaks appearing due to resonant tunneling of Cooper pairs as a function of both V and V_g. The data is measured while a small magnetic field $H \approx 23$ mT $\lesssim H_\mathrm{c}^\mathrm{Al}$ was applied. Right: The same data as a contour plot with a background subtracted, showing clear diamond shaped pattern.

$$V = \frac{1}{2} C_\Sigma V \pm C_\mathrm{g} V_\mathrm{g} \pm Q_0 - e = 0 \tag{5.1}$$

for the necessary resonant condition in a symmetric SET. Here $C_\Sigma = 2C + C_\mathrm{g}$ and C_g is the gate capacitance. Q_0 is the charge on the island before the tunnelling event, i.e., Q_0 is e or $2e$. This equation yields diamond shaped pattern in (V, V_g) plane for the resonances (see Fig. 5.4). The resonance tunnelling itself is not enough to carry a current since it only charges the island with $2e$. This excess charge has to be carried out by another process in the external circuit before a next resonance tunnelling event can take place. This again needs inelastic tunnelling of quasiparticles, whose rate depends greatly on the electromagnetic environment. The environment can be modelled as an infinite number of harmonic LC-oscillators, which can represent any kind environment. This leads to 'P(E)'-theory where Gaussian like P(E) function describes the probability of the system to emit or absorb energy [52]. The resonance peaks appearing in measured

data at $V \lesssim 0.9$ meV are plotted in Fig.5.4 as a function of both V and V_g. Obtained 3D-plot is shown on the left and the right figure shows the same data as a contour plot with the background substracted and it explicitly demonstrates the diamond shaped pattern of the resonant tunnelling of Cooper pairs. If let Q_0 in Eq. 5.1 be either e or $2e$, i.e., assumed the e-periodicity of the structure, the spacing of the measured pattern in the direction of V yields $E_C \approx 34$ μeV, which agrees with the value $E_C \sim 38$ μeV estimated earlier for that sample. The height of the resonances agrees also well with the P(E) theory.

5.2 Elastic cotunneling of quasiparticles, q-MQT

In the I-V curves 5.2 another feature is also visible as a smooth broader peak in the baselines. In Figure 5.5 the voltage dependence of this baseline peak is shown in various magnetic fields ranging from $H = 0$ to $H \gtrsim H_c^{Al}$. The baseline was obtained by averaging the current over the bias range smaller than the spacing of resonance peaks and over the whole V_g range at certain bias voltage. Therefore the supercurrent is also unrealistically smeared in the figure 5.5.

In figure 5.6 comparison between the conductance peak of the baseline of the various samples and the gap of aluminium, obtained by measuring the magnetic field dependence of a single Al-Al junction, clearly shows that the peak follows the voltage determined by $V = 2\Delta_{Al}/e$. As well as the height of the step in baseline follows the gap of aluminum as seen in figure 5.7.

Several processes are known to produce structures in the IV of SSET at bias voltages below the quasiparticle branch, but most of them are in fact excluded in this case by the fact that they leave an excitation on the island. This is forbidden, since at about $2\Delta_{Al}/e$ the system cannot provide enough energy to break the Nb Cooper pairs. Therefore, only two processes are left: the AA cycle and elastic co-tunneling. The first one can be described as follows: two quasiparticles are created in the left electrode and they tunnel to form a Cooper pair on the island. (Equivalently: one electron-like quasiparticle is Andreev-reflected as a hole-like quasiparticle through the left junction,

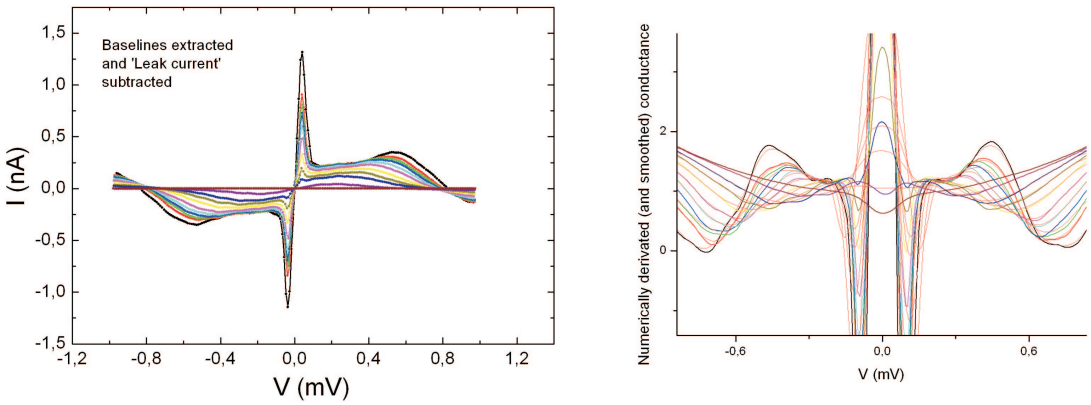

Figure 5.5: Left: The baseline measured at several different magnetic fields ranging from $H = 0$ (highest absolute value of current) to $H \gtrsim H_c^{\mathrm{Al}}$ (lowest absolute value of current). The baseline was obtained by averaging over the resonance peaks, and taking the mean value of the current over whole period of the gate voltage. Right: Derivative of the baseline (conductance). Peaks in the conductance indicating sudden raise in the current as a function of applied magnetic field and bias voltage. The peaks moves towards zero bias voltage while increasing magnetic field.

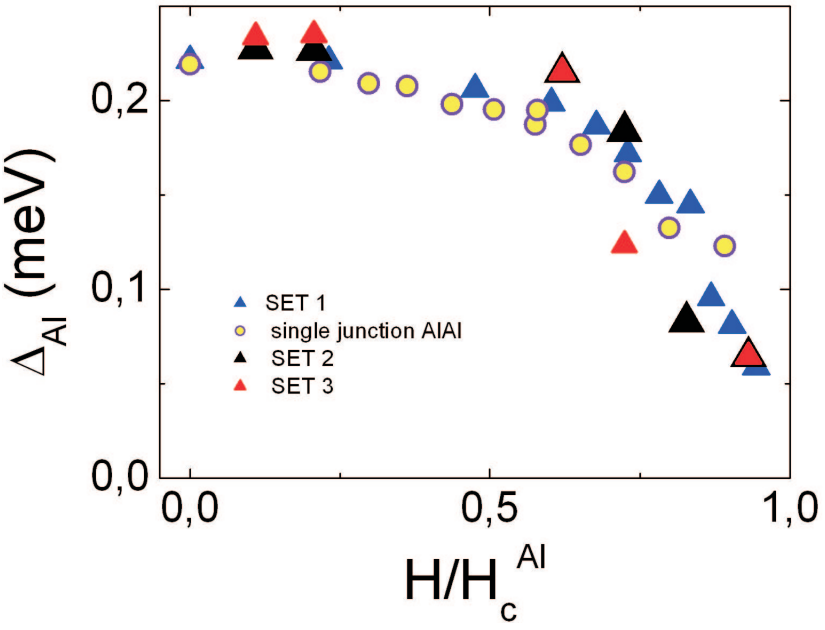

Figure 5.6: Comparison between the position of the conductance peak in V_{b} and the gap of aluminum on a single Al/Al junction at various magnetic fields.

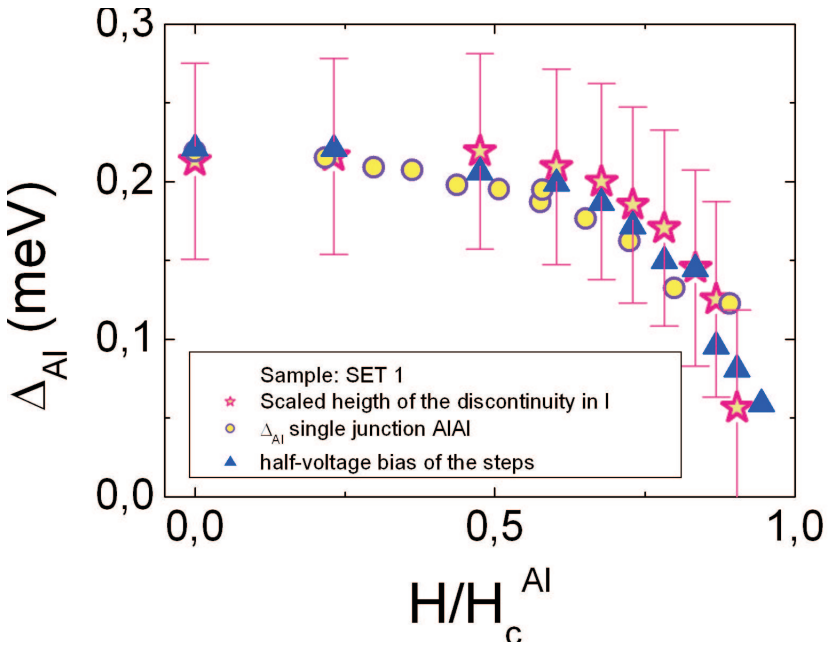

Figure 5.7: The height of the step in the baseline. Circles indicates the gap of the aluminum and the stars relative height of the step, as a function of the applied magnetic field. Triangles follow the step position as in figure (5.6).

with the creation of a Cooper pair propagating to the right in the island.) Then the same Andreev-like process happens at the right junction, resulting in an electron-like excitation propagating in the right electrode. The energy threshold for each of these processes is Δ_{Al}/e, therefore, neglecting the effect of the charging energy, it follows that the whole AA cycle should become important at about twice the gap of aluminum.

In this case, it would mean that the Andreev-like reflection should be visible also in a single junction. To analyse this, several Al-(AlOx)-Nb single junctions were fabricated and measured. For this structure, the theory of MAR (multiple Andreev reflection) and MPT (multiple-particle tunneling) predict a conductance peak (corresponding to a step in the current) at Δ_{Al}/e for a single Andreev reflection. The general structure predicted by these theories is much more complicated, with peaks at $2\Delta_{\mathrm{Al}}/2ne$, Δ_{Nb}/e, and $(\Delta_{\mathrm{Al}}+\Delta_{\mathrm{Al}})/(2n+1)e$. None of these structures were observed in single-junctions. But, some other leak currents were observed probably due to other processes that cannot be characterized yet. However, it has been checked carefully that the activation voltage for these processes does not depend on the gap of Al (by sweeping the temperature

up to the critical temperature of Al). Therefore, even if they might contribute to the backgroud current in the SSET, they cannot account completely for the variation of the current with the Al gap.

The remaining process, q-MQT (elastic co-tunneling), explains the behavior of the background transport in a following way. An electron-like quasiparticle below the energy gap of Al from left electrode tunnels into the island above the Nb gap as a virtual excitation. It may stay on the island a time comparable to uncertainty principle until it tunnels into the right electrode, above the energy gap of Al as shown in figure 5.8. Under the simplifying assumption that the tunneling matrix elements are real and k-independent, the elastic contribution to the current at zero temperature becomes:

$$I_{(el)} = \frac{1}{eR_{eff}} \int_{\Delta_{Al}}^{\infty} dE_L \int_{\Delta_{Al}}^{\infty} dE_R \frac{E_L E_R}{\sqrt{E_L^2 - \Delta_{Al}^2}\sqrt{E_R^2 - \Delta_{Al}^2}} T^2(E_L E_R)\delta(eV - E_L - E_R). \tag{5.2}$$

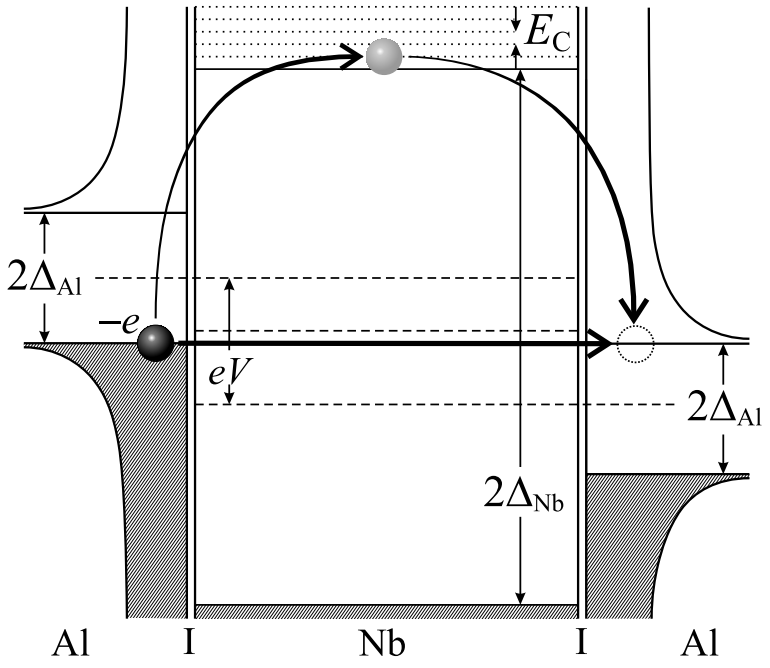

Figure 5.8: Quasiparticle from the left electrode below the gap of Al tunnels to the right electrode above the gap of Al via a virtual excitation on the island. The whole process requires an energy $2\Delta_{Al}$. Dotted lines corresponds to different charging states in the island. The magnetic field and therefore Δ_{Al} dependence of the baseline current becomes easily visualized.

Here $R_{eff} = R_{t,1}R_{t,2}/R_K$, $R_K = h/e^2$ and $R_{t,1}$, $R_{t,2}$ are the resistances of the two junctions, and

$$T(E_L, E_R) = 2\pi \int_{\Delta_{Nb}}^{\infty} dE \frac{E}{\sqrt{E^2 - \Delta_{Nb}^2}} \left[\frac{1}{E_1 + E_L - E_R} - \frac{1}{E_2 - E_k + E_m} \right], \qquad (5.3)$$

where E_1 and E_2 are defined in [53] as changes in charging energy to move a quasiparticle through the left side junction and the right hand junction, respectively.

It can be seen that the first formula (5.2) is analog to the tunneling current between two Al superconductors with effective junction resistance R_{eff} and with an energy-dependent tunnelling matrix element. Also it shows that the elastic current starts at $2\Delta_{Al}$ and the corresponding I-V feature will be step-like. In the limit of charging energy and bias voltages much smaller than the Nb gap, these equations indicates that $\mathrm{T}(E_\mathrm{L}, E_\mathrm{R})$ is independent on the energies E_1 and E_2. When $\mathrm{k_B T} \ll \mathrm{E_C} \ll \Delta_\mathrm{Nb}$ and the spacing between the Coulomb states are small compared to Δ_Nb it makes no difference in the equation (5.2) whether to tunnel via first available Coulomb state or the second, thus making the current gate voltage independent. Furthermore, the equation for the minimum free energy of the quasiparticle excitation at finite temperature

$$D(T) = \Delta(T = 0) - k_\mathrm{B} T ln N_\mathrm{dg} \qquad (5.4)$$

where N_dg describes the number of different possibilities to choose a quasiparticle into the island, suppresses any excitation in the island exponentially. This means that inelastic cotunneling, which is usually dominating, is suppressed $\propto e^{D(T)/k_\mathrm{B}T}$.

5.3 Smearing of the gap

An interesting observation was also that in every sample the steep raise of guasiparticle current at the gap voltage $|V| = 2(\Delta_\mathrm{Nb} + \Delta_\mathrm{Al})$ was very smeared. The Pippard coherence length of Al is $\xi_0^\mathrm{Al} = 1600$ nm, which is extremely large when compared to that of Nb, $\xi_0^\mathrm{Nb} = 38$ nm. For pure metals, the Ginzburg-Landau coherence length $\xi(T) = 0.74\xi_0(1 - T/T_\mathrm{C})^{-1/2}$ will be then dramatically different for Al and Nb at any temperature. In the case of thin films ($d \approx 30 - 40$ nm) it can be assumed that the

mean free path l is limited by surface scattering, therefore $l \approx d$. The Ginzburg-Landau coherence length for dirty films, e.g., thin films, $\xi(T) = 0.855\sqrt{\xi_0 l}(1 - T/T_C)^{-1/2}$ will then be still almost one order of magnitude larger in the case of Al. Although the GL equation is strictly valid only close to the critical temperature, it gives in many situations a good qualitative insight about what happens at low temperatures.

In this case, at T = 0 K it can be seen that the GL coherence length for Nb would be of about $30 - 40$ nm, little less than the film thickness, while for Al it is larger by a factor of ∼7. If one analyses the GL equation in the absence of magnetic fields, with $f = \psi/\psi_\infty$ as the reduced order parameter,

$$\xi^2(T)\Delta f + f - f^3 = 0, \tag{5.5}$$

then for samples with GL coherence length much larger than the thickness of the sample $\xi(T) \gg d$ the order parameter is constant. If it were not constant across the sample, the first term in the GL equation would be $\xi^2(T)\Delta f \approx \xi^2(T)f/d^2 \gg f$, therefore the equation cannot be satisfied. This means that for Al films, the superconducting order parameter is almost constant in a transversal section. In contrast, in Nb films this constraint doesn't hold. Therefore, the order parameter can vary across the sample and still satisfy the GL equation. Hence, there could be regions in the Nb electrode with a (continuously) depressed order parameter (a smeared gap). The current corresponding to tunnelling from or into these regions will appear at a smaller value of the bias voltage.

5.4 Conclusion

It is shown that Nb/AlO_X/Al junctions, with high critical temperature ($T \approx 8.5$) and Josephson coupling, can be fabricated using the conventional self-alignment technique with PMMA-based resists. The measured Nb-based SSETs show the clear signature of the resonant tunneling of Cooper pairs combined with the more smeared signature of elastic cotunneling of quasiparticles, q-MQT, through the barrier of Δ_{Nb}. The inelastic cotunneling usually dominating over the elastic one is suppressed according to equation $\Delta_{Nb} \gg E_C, k_b T$. This virtually yields situation where the density of single

electron state on the island is much smaller than density of Coulomb states, which in general is fullfilled only in the case of quantum dots or semiconductor heterostructures. In figure (5.4) spacing of the measured pattern indicates e-periodicity, which means non-equilibrium quasiparticles being present. One solution for the problem is to use quasiparticle traps, that is, to place a normal metal part in a vicinity of the island therefore offering plenty of single electron states below the gap level.

Chapter 6

Further improvements

The use of Nb offered great improvement as an energy barrier for unwanted quasiparticles. As treated in theory part, the charging Hamiltonian contains also quantity called "offset charge". This continuous quantity takes different values for each device and cooldown and it fluctuates in time with an 1/f spectral density. This effect limites dramatically the usefulness of the device in many applications. For example, digital devices require a perfect control over the gate voltage, therefore the SET cannot be used. Also, this noise imposes severe limits on devices in which parity effects [41] are important: for example (single) microwave photon detectors [36], metrological applications of Cooper pair pumps [39], or Bloch oscillation devices [35, 54]. The effect is also the limiting factor for the sensitivity of low-frequency SET electrometers (currently of the order of $\times 10^{-5} \mathrm{e}/\sqrt{\mathrm{Hz}}$ [42]); the r.f.-SET improves this figure by paying the price of going up to higher frequencies, thus making the device more difficult to operate.

It is believed [43] that this phenomenon is caused partly by the differences in the work functions of the electrodes and the island, and partly by the charge motion in the substrate. The first effect can be eliminated by careful material-engineering: for example, in the case of superconducting SET's, it is shown that enhancing the gap of the island by oxygen doping or lowering the gap of the leads by "quasiparticle traps" creates a barrier for the nonequilibrium tunnel electrons, thus reducing considerably the probability of unequilibrium quasiparticles [44]. Also, in the case of multiple-island devices such as Cooper pair pump the 2e periodicity has not been observed even when

the same precautions (filtering of the leads, quasiparticle traps, low temperatures) as for single-island devices have been taken; rather, the trend in the charging diagram is the coexistence of four 2e honeycomb patterns shifted by 1e along the axis of the gate voltages [45]. This suggests that the effect of the substrate is rather strong and essentially not eliminable through the methods described above. The existing noise measurements in SET's suggest that there is a correlation between the type of substrate used and the minimum sensitivity achieved [55]. A more radical approach to the issue of substrate noise is proposed: to eliminate the substrate itself.

6.1 Suspended single-electron transistor

It is possible to fabricate working high-quality single-electron transistor in which the island is not in contact with the substrate [50]. This new type of device, suspending single-electron transistor (SUSET), has shown well-defined I-V and dI/dV-V features typical for high-quality standard SET's. The fabricated Al-based transistor is shown in Figure 6.1. The height of the island from the substrate is approximately 4-5 μm and the length of the suspending part is about 20 μm. The length of the island is 1μm, and the thickness is less than 100 nm.

6.2 Fabrication of SUSET

The suspended SET was fabricated using conventional two-angle evaporation on a nitridized (300 nm) Si wafer of 500 μm thickness followed by reactive ion etching. The current dose was double compared to SET-on-oxidized-substrate, due to a smaller amount of secondary electrons (see section 3.1). The mask was drawn using a scanning electron microscope (JEOL, JSM 840A) with acceleration voltage of 20 kV. The minimum width of the pattern in the island region was 50 nm; however, the resulting width of the metallic wires after the whole process increased to 100 nm. The resists were developed, and the mask was further cleaned in a reactive ion etcher (AXIC BENCHMARK) at 30 mTorr pressure with 50 sccm flow of O_2 and 48 W RF-power for 30 s,

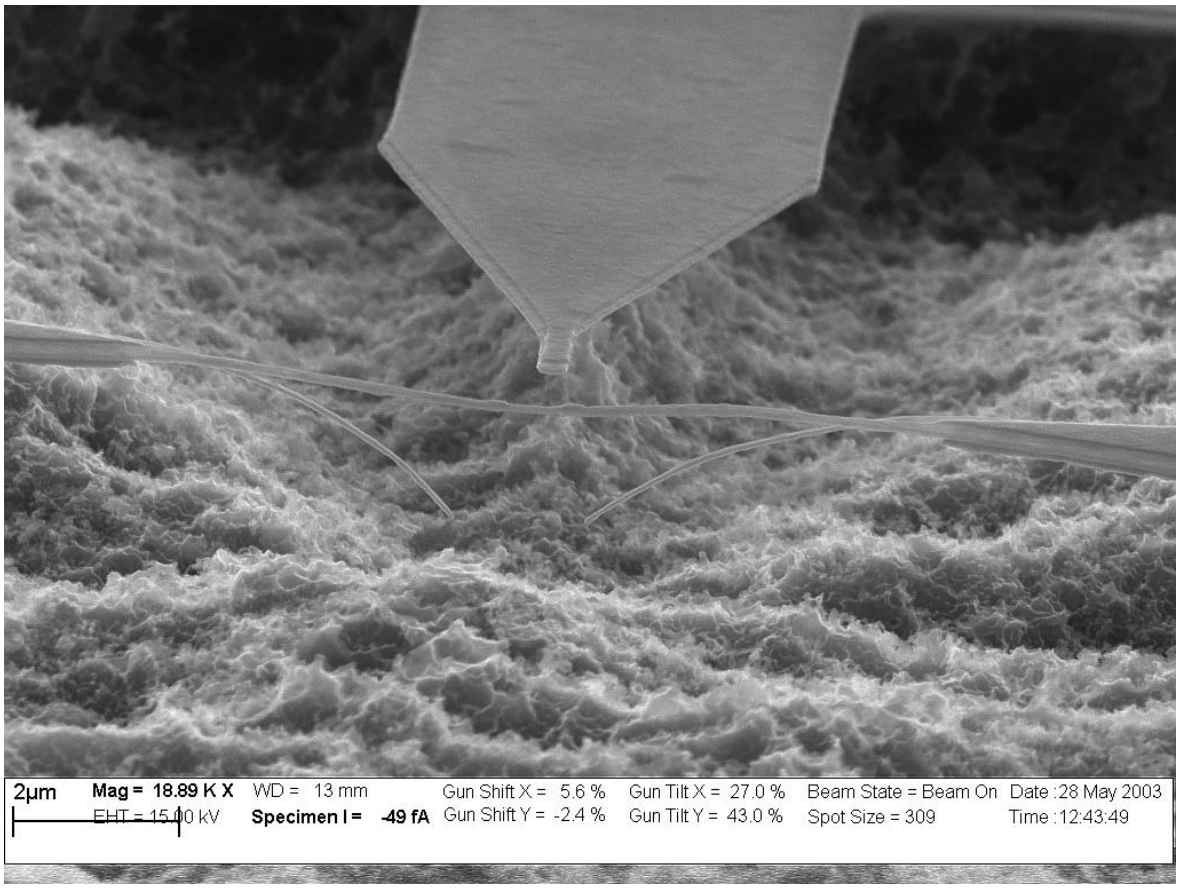

Figure 6.1: *High-magnification SEM image of a suspending single-electron transistor. The tip of the gate electrode (center up) points to the island. The junctions can be seen as two thicker nodular structures along the suspended aluminum wire. The two lines pointing downwards (towards the substrate) are the usual by-products of two-angle evaporation.*

a process that removes the resist leftovers from the SiN_2 surfaces. The aluminum was evaporated in an UHV chamber at pressure of 2–4$\times 10^{-8}$ mbar with an evaporation rate of 0.5 nm/s for both the island and the electrodes. The film, with a thickness of 60 nm, was oxidized between the evaporations in a steady flow of O_2, at a pressure of 20 mbar for three minutes. In the sample presented here, the 45 nm and 60 nm correspond to the thicknesses of the island and the leads, respectively. The process was completed by lift-off, with the sample being slowly heated in acetone up to the boiling point (56°C) and gradually cooled down to room temperature.

Finally the SET was put into a RIE (AXIC BENCHMARK) and etched in a two step process. The power was 60 Watts, and the flow of O_2 and CF_4 was 5 sccm and 10.5 sccm respectively. The first step was anisotropic etch at a pressure of 40 mTorr for 3 minutes (ion bombarment to break the surface of the nitride). The second step (isotropic etch) was at a pressure of 70 mTorr for 7 minutes. The process was on all the time, shift to higher pressure was done on the fly. Table 6.1 captures the essential of the fabrication of SUSET.

Evaporation				
Process	Substance	Angle α	Thickness	Speed
1	Aluminum	+29	600 Å	5Å/s
Oxidation	20 mbar 3 minutes			
2	Aluminum	-29	450 Å	5 Å/s
Etching				
Process	Flow	Pressure	Power	Time
1	O_2 5 sccm	40 mTorr	10 %	3 min
	CF_4 10.5 sccm	40 mTorr	10 %	3 min
2	O_2 5 sccm	70 mTorr	10 %	7 min
	CF_4 10.5 sccm	70 mTorr	10 %	7 min

Table 6.1: *Table of parameters for SUSET. Pressure of etching was changed while process is still running.*

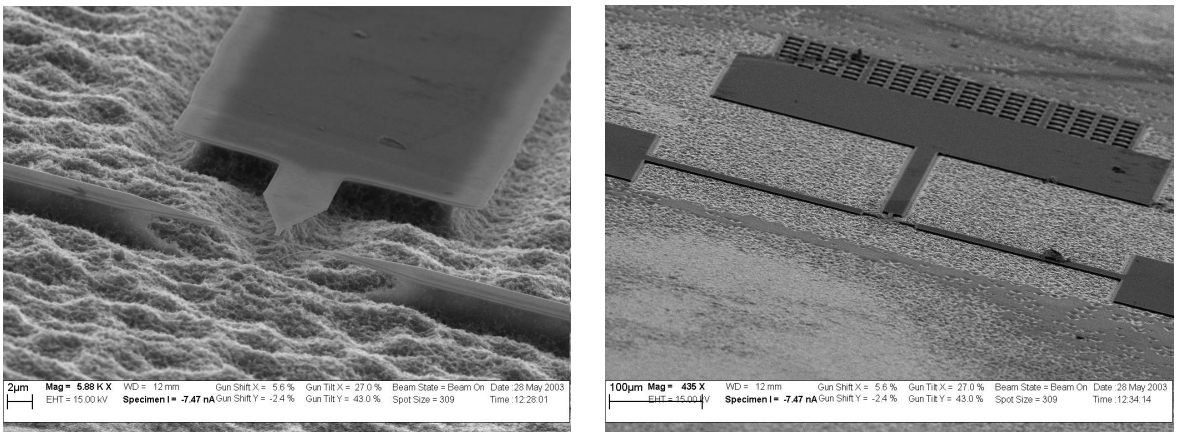

Figure 6.2: A lower-magnification SEM picture of a suspended single-electron transistor, showing the effect of etching on the SiN_2 substrate. The picture at right shows the full large-scale structure, including the bonding pad for the gate.

6.3 Measurement of SUSET

The SUSET was measured in an electrically shielded room using a Nanoway PDR-50 dilution refrigerator with the lines filtered with commercial π-filters at 4.2 K and a combination of π-filters and RC-filters at room temperature, as in previous sections. The conductance was measured using a lock-in amplifier technique. The results are presented in Fig. 6.3. The sample presented here had a room-temperature resistance of $R_n = 73$ kΩ. From the threshold voltage of the quasiparticle branch at 0.755 meV we can determine the gap of Al to be 0.189 meV.

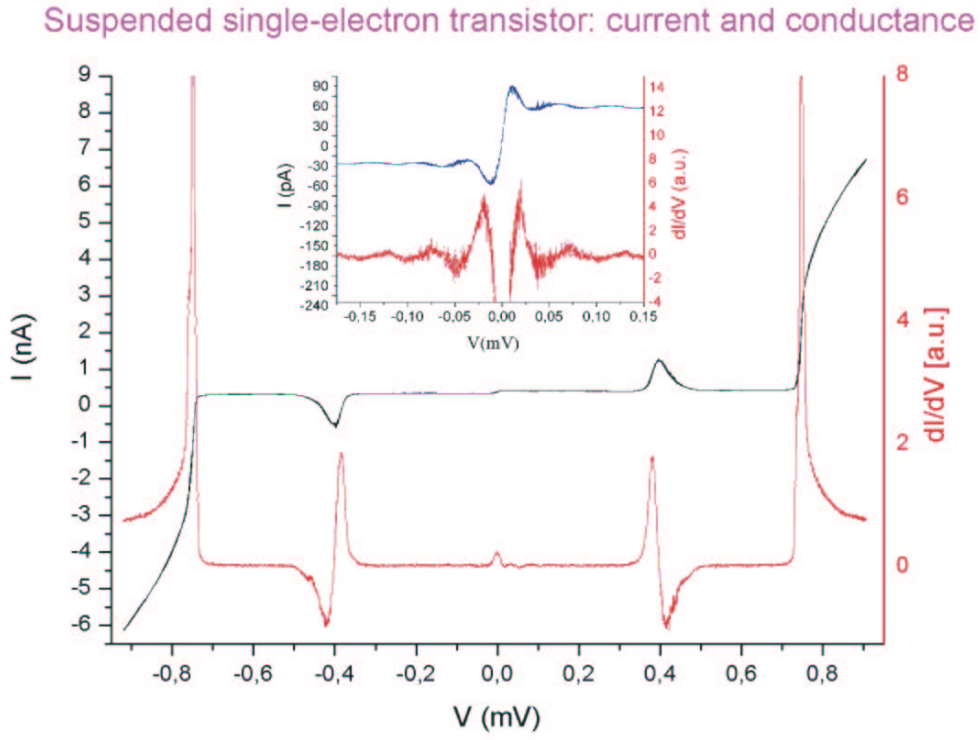

Figure 6.3: Current and conductance as function of bias voltage, showing features of a good-quality SET (Josephson current, JQP, and quasiparticle conductance edge). The inset is a low-bias voltage detail, with a better visible Josephson effect and mild Cooper pair resonant peaks in the current.

The charging energy of the sample was derived from the Coulomb-blockade conductance measured at 4.2 K; we found a change in the zero-bias conductance peak

$\delta G/G_T = 1.24\%$, yielding a charging energy $E_c = e^2/2C_\Sigma = 13.5\mu$eV, where $C_\Sigma = C_1 + C_2 + C_g$ is the usual definition for the total capacitance of the island.

The critical Josephson current from Fig. 6.3 is approximately 70 pA; switching-current measurements, which are more precise, yielded a value $I_c = 61$ pA for this sample. This corresponds to a quite small Josephson energy $E_J = \hbar I_c/2e = 0.13\mu$ eV.

The Ambegaokar-Baratoff formula gives $E_J = R_K\Delta_{\mathrm{Al}}/8R_n = 8.3\mu$ eV, significantly larger than the measured value. These are a well-known discrepancies for SET's, caused by the sensitivity of the Josephson effect in small junctions to the external electromagnetic environment [46]. They occur when E_c is larger or of the same order of magnitude as E_J (therefore the phase of the island is not a good quantum number and the current has strong fluctuations), which is indeed the case for our sample.

In Fig. 6.3 the two symmetric peaks in the current are due to a combined Josephson and quasiparticle (JQP) tunneling in the junctions; this effect is predicted to happen at a bias voltages $2\Delta_{\mathrm{Al}} + E_{\mathrm{C}} \leq eV \leq 2\Delta_{\mathrm{Al}} + 3E_{\mathrm{C}}$ [47]. For our sample, this gives 0.391 meV $\lesssim eV \lesssim$ 0.418 meV, in excellent agreement with the position of the peak in the experimental data (Fig. 6.3). The JQP features are quite broad, as expected from the theory of this process for samples with small E_c/Δ [48].

Finally, a measurement at low bias voltages (inset of Fig. 6.3) reveals a finer structure of resonances in the current, corresponding to oscillations in the conductance. According to the theory of resonant tunneling of Cooper pairs [49], the spacing between consecutive peaks peaks should be $4E_{\mathrm{C}}$, i.e., 54 μeV. Although the data were quite noisy, it was still possible to estimate the distance between peaks as being indeed 50-60 μeV. The SUSET is affected by temperature in the same way as conventional SET's. Fig. 6.4 presents I-V measurements from 0.2 K to about 0.9 K, close to the critical temperature of Al. The low-temperature features get more rounded and they are displaced towards lower bias voltages, in agreement with the decrease of the gap of Al.

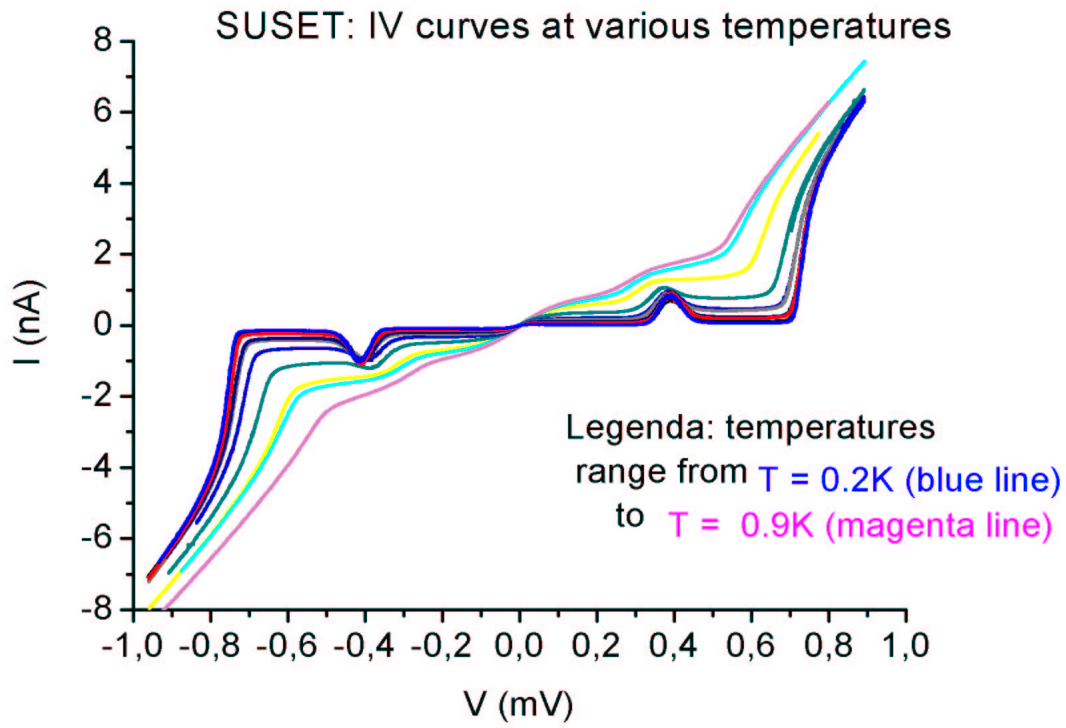

Figure 6.4: I-V characteristics as a function of temperature. The sharpest features correspond to T = 0.2 K; the temperature was then raised close to the critical temperature of Al.

6.4 Conclusion of Suset

In conclusion, high quality Al-based superconducting suspended SET was fabricated and measured. Any decrease of the quality was not observed due to the extra etching process. On a contrary, the SET's showed remarkable tolerance under thermal cycling and athmospheric condition. Therefore, we believe that this new device can be useful in applications that require a precise control of the nonequilibrium charge on the islands.

Bibliography

[1] M. Tinkham, *Introduction to Superconductivity*, second edition, McGRAW-HILL, (1996)

[2] I. Giaever, *Phys. Rev. Lett*, **5**, 147, 464 (1960).

[3] G. J. Dolan, *Offset masks for lift-off photoprocessing*, Appl. Phys. Lett, **31**, 337, (1977).

[4] F. Mandl, *Quantum mechanics*, John Wiley & Sons Ltd, Baffins Lane, (1992)

[5] Alexey B. Pavolotsky, Thomas Weimann, Hansjörg Scherer, Vladimir A. Krupenin, Jürgen Niemeyer, and Alexander B. Zorin *Multilayer technique developed for fabricating Nb-based single-electron devices* J. Vac. Sci. Technol. B 17, 230 (1999).

[6] P. Dupos, P. Charlat, Th. Crozes, P Paniez, and B.Pannetier, *Thermostable trilayer resist for niobium lift-off*, J. Vac. Sci. Technol. B **18**, 122 (2000).

[7] Y. Harada, D. B Haviland, P. Delsing, C. D. Chen, and T. Claesson *Fabrication and measurement of a Nb based superconducting single electron transistor*, Appl. Phys. Lett. **65**, 636 (1994).

[8] Nam Kim, Klavs Hansen, Jussi Toppari, Tarmo Suppula, and Jukka Pekola, *Fabrication of mesoscopic superconducting Nb wires using conventional electron beam lithographic techniques*, J. Vac. Sci Technol. B **20**(1),(2002) **65**, 636 (1994).

[9] *Communications at the* 23^{rd} *International Conference on Low Temperature Physics*, Hirosima, Japan, August $20 - 27$ (2002)

[10] Panu Koppinen, Master Thesis, *Bias and temperature dependence analysis of the tunneling current of normal metal-insulator-normal metal tunnel junctions*, University of Jyväskylä, (2003)

[11] B.D.Josephson, *Phys. Letters 1*, 251 (1962)

[12] V.L. Ginsburg and L.D Landau, *Zh. Eksperim. i Teor. Fiz*, **20**,1064 (1950)

[13] D. V. Averin and K. K. Likharev, J. Low Temp. Phys. **62**, 345 (1986)

[14] T. A. Fulton and G. J. Dolan, Phys. Rev. Lett. **59**, 109 (1987)

[15] M. H. Devoret, R. J. Schoelkopf, Nature **406, 1039**

[16] Marko Savolainen, Pro Gradu, *Yksittäisten elektronien ja Cooperin parien mittaaminen elektrometrillä metallisissa nanorakenteissa*, University of Jyväskylä, (2003)

[17] Philippe Joyez, These de Doctorat, *Le transistor a une paire de Cooper: Un systeme quantique macroscopique*, l'UNIVERSITE PARIS 6, (1995)

[18] Y.Nakamura, Y.A.Pashkin, and Tsai, Nature **398**, 786 (1999)

[19] J.R. Friedmann, V. Patel, W. Chen, S.K. Tolpygo, and J.E. Lukens, Nature **406**, 43 (2000)

[20] C.H. van der Wal, A.C.J. ter Haar, F.K. Wilhelm, R.N. Schouten, C.J.P.M Harmans, and J. E. Mooij, Science **290**, 773 (2000)

[21] D. Vion, A. Aassime, A. Cottet, P. Joyez, H. Pothier, C. Urbina, D. Esteve, and M.H. Devoret, Science **296**, 886 (2002)

[22] Y. Makhlin, G. Schön, and A. Shnirman, Rev. Mod. Phys. **73**, 357 (2001)

[23] D. Averin, Solid State Commun. **105**, 659 (1998)

[24] A.B. Zorin, Phys.Rev.Lett. **86**, 3388 (2001)

[25] J.P. Pekola, J.J. Toppari, M. Aunola, M. T. Savolainen, and D. V. Averin, Phys. Rev. B **60**, R9931 (1999)

[26] K.K Likharev and A.B. Zorin, J. Low Temp. Phys. **59**, 347 (1985)

[27] J.P. Pekola and J.J. Toppari, Phys. Rev. B **64**, 172509 (2001)

[28] R. Fazio, F.W.J. Hekking, and J.P. Pekola, Phys. Rev. B (2003)

[29] D. H. Douglass Jr., IBM Journal of research and development, Vol. 6, Nr 1, page 44 (1962)

[30] F. Neumann, G.L. Ingold and H. Grabert, Phys. Rev. B **50**, 12811 (1994)

[31] L.J. Geerligs, V.F. Anderegg, J. Romijn, and J.E. Mooij, Phys.Rev.Lett. **65**, 377 (1990)

[32] D. V. Averin and K. K. Likharev, J. Low Temp. Phys. **62**, 345 (1986).

[33] T. A. Fulton and G. J. Dolan, Phys. Rev. Lett. **59**, 109 (1987).

[34] R. J. Schoelkopf, P. Wahlgren, A. A. Kozhevnikov, P. Delsing, and D. E. Prober, Science **280**, 1238 (1998).

[35] L. S. Kuzmin and D. B. Haviland, Phys. Scr. T **42**, 171 (1992).

[36] J. M. Hergenrother, J. G. Lu, M. T. Tuominen, D. C. Ralph, and M. Tinkham, Phys. Rev. B **51**, 9407 (1995); S. Komiyama, O. Astafiev, V. Antonov, T. Kutsuwa, and H. A. Hirai, Nature **403**, 405 (2000).

[37] Y. Nakamura, Y. A. Pashkin, and J. S. Tsai, Nature, **398**, 786 (1999); J. E. Mooij, T. P. Orlando, L. Levitov, L. Tian, C. H. van der Val, and S. Lloyd, Science **285**, 1036 (1999); J. R. Friedman, V. Patel, W. Chen, S. K. Tolpygo, and J. E. Lukens, Nature **406**, 43 (2000); D. Vion, A. Aassime, A. Cottet, P. Joyez, H. Pothier, C. Urbina, D. Esteve, and M. H. Devoret, Science **296**, 886 (2002); I. Chiorescu, Y. Nakamura, C. J. P. M. Harmans, and J. E. Mooij, Science **299**, 1869 (2003);

Yu. A. Paskin, T. Yamamoto, O. Astafiev, Y. Nakamura, D. V. Averin, and J. S. Tsai, Nature **421**, 823 (2003).

[38] Y. Makhlin, G. Schön, and A. Shnirman, Nature **386**, 305 (1999); Yu. Makhlin, G. Schön, and A. Shnirman, Rev. Mod. Phys. **73**, 357 (2001);

[39] K. K. Likharev and A. B. Zorin, J. Low Temp. Phys., **59**, 347 (1985); J. P. Pekola, J. J. Toppari, M. Aunola, M. T. Savolainen, and D. V. Averin, Phys. Rev. B **60** R9931 (1999).

[40] J. P. Pekola and J. J. Toppari, Phys. Rev. B **64** 172509 (2001); R. Fazio, F. W. J. Hekking, and J. P. Pekola, Phys. Rev. B (2003), in press.

[41] M. Tinkham, *Introduction to Superconductivity*, 2nd ed. (McGraw-Hill Inc., New York, 1996); M. T. Tuominen, J. M. Hergenrother, T. S. Tighe, and M. Tinkham, Phys. Rev. Lett. **69**, 1997 (1992).

[42] E. N. Visscher, S. M. Verbrugh, J. Lindeman, P. Hadley, and J. E. Mooij, Appl. Phys. Lett. **66**, 305 (1995); V. A. Krupenin, D. E. Presnov, M. N. Savvateev, H. Scherer, A. B. Zorin, and J. Niemeyer, J. Appl. Phys. **84**, 3212 (1998).

[43] M. H. Devoret, R. J. Schoelkopf, Nature **406**, 1039 (2000).

[44] P. Joyez, P. Lafarge, A. Filipe, D. Esteve, and M. H. Devoret, Phys. Rev. Lett. **72**, 2458 (1994); J. Aumentado, M. W. Keller, J. M. Martinis, and M. H. Devoret, cond-mat/0308253.

[45] J.J. Toppari, J.M. Kivioja, J.P. Pekola and M.T. Savolainen, *Turnstile behaviour of the Cooper pair pump*, J. Low Temp. Phys. **136** 57 (2004).

[46] P. Joyez, D. Vion, M. Götz, M. H. Devoret, and D. Esteve, Journal of Superconductivity, **12**, 757 (1999); A. Steinbach, P. Joyez, A. Cotet, D. Esteve, M. H. Devoret, M. E. Huber, and J. M. Martinis, Phys. Rev. Lett. **87**, 137003 (2001).

[47] T. A. Fulton, P. L. Gammel, D. J. Bishop, L. N. Dunkleberger, and G. J. Dolan, Phys. Rev. Lett. **63**, 1307 (1989); Y. Nakamura, C. D. Chen, and J. S. Tsai, Phys. Rev. B **53**, 8234 (1996).

[48] S. L. Pohlen, R. J. Fitzgerald, and M. Tinkham, Physica B **284-288**, 1812 (2000).

[49] A. Maassen van den Brink, A. A. Odintsov, P. A. Bobbert, and G. Schön, Z. Phys. B **85**, 459 (1991); D. B. Haviland, Y. Harada, P. Delsing, C. D. Chen, and T. Claeson, Phys. Rev. Lett. **73**, 1541 (1993); Y. Harada, D. B. Haviland, P. Delsing, C. D. Chen, and T. Claesson, Appl. Phys. Lett. **65**, 636 (1994).

[50] G. S. Paraoanu and A. M. Halvari , *Applied Physics Letters* **86**, 093101 (2005)

[51] J.J. Toppari, G.S. Paraoanu, A.M. Halvari, and J.P. Pekola, *Elastic cotunnelling of quasiparticles in superconducting Al/Nb/Al single electron transistors*, cond-mat/0311148 (2003) (Submitted).

[52] Ingold, G.-L. and Nazarov, Yu. V., *Charge tunneling rates in ultrasmall junctions, in single charge tunneling, Coulomb blockade phennomena in nanostructures*, edited by H.Grabert and M.H. Devored (Plenum, New York, 1992), p.21.

[53] D. V. Averin and Yu. V. Nazarov, Phys. Rev. Lett **65**, 2446 (1990).

[54] J. Delahaye, J. Hassel, R. Lindell, M. Sillanpää, M. Paalanen, H. Seppä, and P. Hakonen *Science* **299**, 1045 (2003)

[55] A. B Zorin, F. -J. Ahlers, J. Niemeyer, T. Weiman, H. Wolf, V. A. Krupenin, and S. V. Lotkhov, *Phys. Rev. B* **53**, 13682 (1996); N. M. Zimmerman, J. L. Cobb, and A. F. Clark, *ibid.* **56**, 7675 (1997)

[56] G. S. Paraoanu and A. Halvari, *Fabrication and measurement of superconducting Nb-based junctions*, Rev. Adv. Mater. Sci., 5 265 (2003).

Appendix A

Matrix presentation of Hamiltonian

Total Hamiltonian when quasiparticle excitations are excluded is

$$H_{\mathrm{C}} + H_{J1} + H_{J2},$$

where

$$H_{Ji} = -E_{Ji} \cos \varphi_i,$$

$$H_C = E_C (n - n_{\mathrm{g}})^2$$

and $E_C = (2e)^2/2C_\Sigma$. With operator change

$$\hat{\varphi}_1 = \tfrac{\hat{\varphi}}{2} + \hat{\theta}$$

$$\hat{\varphi}_2 = \tfrac{\hat{\varphi}}{2} - \hat{\theta},$$

where states $|\theta\rangle$ form a complete set so that

$$|n\rangle = \int |\theta\rangle\langle\theta|n\rangle d\theta = \frac{1}{\sqrt{2\pi}} \int e^{i\theta n} |\theta\rangle d\theta,$$

the total Hamiltonian gets the form

$$H = E_C (n - n_{\mathrm{g}})^2 - (E_{J1} + E_{J2}) \cos \frac{\varphi}{2} \cos \theta - (E_{J1} + E_{J2}) \sin \frac{\varphi}{2} \sin \theta.$$

The charging energy part in the matrix of the Hamiltonian is diagonal in the chosen $|n\rangle$ basis. In the calculation of the Josephson coupling, off-diagonal elements

$$\langle n'| - \sum_{\mathrm{i}=1}^{2} E_{\mathrm{J1}} \cos \varphi_{\mathrm{i}} |n\rangle$$

can be simplified with the help of following equations

$$\cos\theta = 1/2(e^{i\theta} + e^{-i\theta})$$

$$\sin\theta = 1/2i(e^{i\theta} - e^{-i\theta}).$$

The off-diagonal element gets the form

$$\langle n'|(E_{J1} - E_{J2})\sin\frac{\varphi}{2}\frac{1}{2i}(e^{i\theta} - e^{-i\theta})\frac{1}{\sqrt{2\pi}}\int e^{i\theta n}|\theta\rangle d\theta$$

$$\langle n'| - (E_{J1} - E_{J2})\cos\frac{\varphi}{2}\frac{1}{2}(e^{i\theta} + e^{-i\theta})\frac{1}{\sqrt{2\pi}}\int e^{i\theta n}|\theta\rangle d\theta$$

$$= \langle n'|(E_{J1} - E_{J2})\sin\frac{\varphi}{2}\frac{1}{2i}\left[\frac{1}{\sqrt{2\pi}}\int e^{i\theta(n+1)}|\theta\rangle d\theta - \frac{1}{\sqrt{2\pi}}\int e^{i\theta(n-1)}|\theta\rangle d\theta\right]$$

$$\langle n'| - (E_{J1} + E_{J2})\cos\frac{\varphi}{2}\frac{1}{2i}\left[\frac{1}{\sqrt{2\pi}}\int e^{i\theta(n+1)}|\theta\rangle d\theta - \frac{1}{\sqrt{2\pi}}\int e^{i\theta(n-1)}|\theta\rangle d\theta\right]$$

$$= \langle n'|(E_{J1} - E_{J2})\sin\frac{\varphi}{2}\frac{1}{2i}\left[|n+1\rangle - |n-1\rangle\right] - \langle n'|(E_{J1} + E_{J2})\cos\frac{\varphi}{2}\frac{1}{2}\left[|n+1\rangle + |n-1\rangle\right]$$

$$= \langle n'|(E_{J1} - E_{J2})\sin\frac{\varphi}{2}\frac{1}{2i}|n+1\rangle - \langle n'|(E_{J1} + E_{J2})\cos\frac{\varphi}{2}\frac{1}{2}|n+1\rangle$$
$$-\langle n'|(E_{J1} - E_{J2})\sin\frac{\varphi}{2}\frac{1}{2i}|n-1\rangle - \langle n'|(E_{J1} + E_{J2})\cos\frac{\varphi}{2}\frac{1}{2}|n-1\rangle.$$

If it is assumed that $E_{\mathrm{J1}} = E_{\mathrm{J2}} = E_{\mathrm{J}}$, then

$$= -\langle n'|E_{\mathrm{J}}\cos\frac{\varphi}{2}|n+1\rangle - \langle n'|E_{\mathrm{J}}\cos\frac{\varphi}{2}|n-1\rangle,$$

so that

$$\langle n'|H_{\mathrm{J1}} + H_{\mathrm{J2}}|n\rangle$$
$$= -E_{\mathrm{J}}\cos\frac{\varphi}{2}\delta_{\mathrm{n'},\mathrm{n}+1} - E_{\mathrm{J}}\cos\frac{\varphi}{2}\delta_{\mathrm{n'},\mathrm{n}-1}.$$

Finally, the Hamiltonian in the $|n\rangle$ basis of the three states $|-1\rangle, |0\rangle$, and $|1\rangle$ becomes

$$H = \begin{pmatrix} E_{\mathrm{C}}(-1-n_{\mathrm{g}})^2 & -E_{\mathrm{J}}\cos(\frac{\varphi}{2}) & 0 \\ -E_{\mathrm{J}}\cos(\frac{\varphi}{2}) & E_{\mathrm{C}}n_{\mathrm{g}}^2 & -E_{\mathrm{J}}\cos(\frac{\varphi}{2}) \\ 0 & -E_{\mathrm{J}}\cos(\frac{\varphi}{2}) & E_{\mathrm{C}}(1-n_{\mathrm{g}})^2 \end{pmatrix}$$